ACTA MATERIALIA TRANSYLVANICA

Material Sciences Publications

Volume 1, Issue 2

ERDÉLYI MÚZEUM-EGYESÜLET
Kolozsvár
2018

A folyóirat megjelenését támogatta a Magyar Tudományos Akadémia, a Bethlen Gábor Alapkezelő Zrt. és az EME Műszaki Tudományok Szakosztálya / The publication of this magazine was supported by the Hungarian Academy of Sciences, by the Bethlen Gábor Fund and by the TMS – Department of Engineering Sciences

Kiadó / Publisher: Erdélyi Múzeum-Egyesület
Felelős kiadó / Responsible publisher: Biró Annamária
Olvasószerkesztő / Proofreader: Szenkovics Enikő (magyar), David Speight (English)
Szerkesztőségi titkár / Editorial secretary: Kisfaludi-Bak Zsombor
Műszaki szerkesztő / DTP: Szilágyi Júlia
Borítóterv / Cover: Könczey Elemér
Nyomdai munkálatok / Printed at: F&F International Kft., Gyergyószentmiklós

ISSN 2601-1883, ISSN-L 2601-1883
DOI: 10.33924/amt-2018-02
Online elérhető / online available at: https://eda.eme.ro/handle/10598/30356
A folyóirat honlapja / The journal webpage: http://www.eme.ro/publication/acta-mat/mat-main.htm

Az *Acta Materialia Transylvanica. Anyagtudományi Közlemények* az Erdélyi Múzeum-Egyesület (EME) Műszaki Tudományok Szakosztályának folyóirata, amely az anyagtudományok területéről közöl tudományos közleményeket: szakcikkeket, összefoglalókat (szemléket), tanulmányokat. A folyóirat célja összképet adni kiemelten a Kárpát-medencei kutatási irányokról, tudományos eredményeiről, s ezt széles körben terjeszteni is. A folyóirat az EME felvállalt céljaihoz híven a magyar szaknyelv ápolását is támogatja, így a nyomtatott folyóirat magyar nyelven jelenik meg, mely az Erdélyi digitális adattárban elérhető (https://eda.eme.ro/handle/10598/30356). A széles körű nemzetközi terjesztés érdekében a folyóirat teljes angol nyelvű változatát is közzétesszük.

Acta Materiala Transylvanica – Material Sciences Publications – is a journal of the Technical Sciences Department of the Transylvanian Museum Society, publishing scientific papers, issues, reviews and studies in the field of material sciences. Its mission is to provide and disseminate a comprehensive picture focusing on research trends and scientific results in the Carpathian basin. In accordance with the general mission of the Transylvanian Museum Society it aims to support specialized literature in Hungarian. The printed version of the journal is published in Hungarian and is available in the Transylvanian Digital Database (https://eda.eme.ro/handle/10598/30356). However, we would like to spread it internationally, therefore the full content of the journal will also be available in English.

Tartalom / Content

Acta Materialia Transylvanica 1/2. (2018) 65–72.
https://doi.org/10.2478/amt-2018-0022
Hungarian: ~~https://doi.org/10.2478/amt-2018-0021,~~
https://doi.org/10.33923/amt-2018-0021
Corrected: 29.08.2023.

Comparative Study of Roman Iron Slags Discovered in the Roman Auxiliary Fort and Settlement of Călugăreni

Enikő BITAY[1], Irén KACSÓ[2], Szilamér Péter PÁNCZÉL[3], Erzsébet VERESS[4]

[1] *Sapientia Hungarian University of Transylvania, Faculty of Technical and Human Sciences, Târgu-Mureş, Romania, ebitay@ms.sapientia.ro*

[2] *National Institute for Research and Development of Isotopic and Molecular Technologies (INCDTIM), Cluj-Napoca, Romania, iren.kacso@gmail.com*

[3] *Mureş County Museum, Târgu-Mureş, Romania, pszilamer@yahoo.com*

[4] *Transylvanian Museum Society, Cluj-Napoca, Romania, veresserzsebet@gmail.com*

Abstract

Iron slag samples unearthed at the eastern border of Roman Dacia, in the auxiliary fort and the military settlement of Călugăreni (Mikháza) are investigated by macroscopic inspection, optical microscopy (OM) and FTIR spectroscopy in order to comparatively characterize their macro- and microstructure as well as their mineralogical composition. During the recent archaeological excavations, a large number of iron artefacts were discovered together with a great quantity of iron slag fragments. The present paper focuses on the data obtained from 17 slag samples.

Keywords*: iron slags, macroscopic investigation, optical microscopy, FTIR spectroscopy.*

---

1. Introduction

Among other resources, the procurement of rich ore and salt mines were a determining factor in the decision of the Romans to conquer Dacia. In the territory of the defeated Dacian kingdom a Roman province was organized at the beginning of the 2nd century, and continued to develop until the middle of the 3rd century. After the conquest the border defense system (*limes*) of the new province was established, similar to other parts of the Roman Empire. On the borderline – the outer defensive line of the circular defence system – auxiliary units were stationed [1,2], while in the central part and on the more vulnerable western border the auxiliary units and legions were also positioned. Due to the frequency of barbaric incursions and the economic and political instability of the Empire, the emperor Aurelianus abandoned the province at the beginning of the 270's and withdrew the army to the Danube defence line.

In the line of the *limes* in today's Mureş (Maros) County, we know of three auxiliary forts, along with their adjoining settlements which are located in today's Brâncoveneşti (Marosvécs), Călugăreni (Mikháza) and Sărăţeni (Sóvárad).

The Călugăreni auxiliary fort played an important strategic role in the defence of the Niraj (Nyárád) valley. During the 2nd and 3rd century, the more than forty hectares site was the most important economic and military centre in the region. Based on archaeological prospections and geophysical surveys, the ground plan and the layout of the 2.3-hectare large rectangular fort (*castrum / castellum*) strictly followed the rules of Roman military architecture.

The fort was oriented NE-SW and is located in the central part of the archaeological site. [3, 4] The settlement (*vicus militaris*) developed around it and is located in the western part of the present village and the arable land between Călugăreni and Dămieni (Deményháza). (Figure 1. and 2.)

The main aim of the current excavation is to investigate the headquarter building (*principia*) located at the crossroads of major roads of the fort and a residential area from the *vicus*.

Figure 1. *The excavation areas at the (1) vicus and the (2) auxiliary fort (made by Nándor Laczkó)*

Figure 2. *Virtual reconstruction of the site (made by Zsolt Vasáros)*

2. Experimental

2.1. Brief review of the samples

The iron slag samples studied are presented in **Table 1.** Most of them were unearthed at the residential area discovered at the Călugăreni military settlement (vicus) during the excavations performed in 2013–2014, situated on the trench C, C1, C2 of the site. The finds discovered after 2015 belong to the trenches A2, A5, A2015 and A6 from the 3rd century phase of the headquarter building (principia). In the selection of the samples chosen for this study, besides the archaeological relevance, the assurance of the adequate probe quantity in order to complete the planned investigations was considered.

Macroscopic characterization of the samples was performed by visual examination, in daylight, under a magnifying glass of 5x magnifying power. The macrophotos were obtained using a LUMIX TS7 digital camera of 20.4 Megapixels, at the same time and in the same conditions, and are presented in **Figure 3.** and **4.**

Due to the relatively small number of specimens selected, the classification of the probes associated with the excavation trench and the context and macroscopic characteristics was not possible.

The samples collected on the vicus territory typically are partially glassy, with dark grey and/or black zones on the outer surfaces, containing various quantity of differently sized gas inclusions (lunkers, vesicles) and iron inclusions (metallic droplets).

The macroscopic morphology of the samples 2008, 2155, 2355, 2356, 4009 and 4264 is pumiceous (spongy) and pronouncedly vesicular (with many gas lunkers) assuring their low density. They are very heterogeneous, with greyish, reddish, blackish, clayish-yellow with more or less crystallized or glassy zones on the surface. In

Table 1. *The iron slag samples*

No.	Small find no.	Trench	Context	Excav. year
Finds from the *vicus*				
1	2008	C	2000	2013
2	2155	C	2001	2013
3	2318	C	2005	2013
4	2342	C	2005	2013
5	2355	C	2009	2013
6	2356	C	2009	2013
7	4009	C2	2039	2014
8	4137	C1	2034	2014
9	4169	C2	2039	2014
10	4222	C1	2038	2014
11	4251	C1	2035	2014
12	4264	C1	2038	2014
Finds from the *principia*				
13	10218	A2	109	2015
14	10532	A5	250	2016
15	10661	A5	339	2016
16	10673	A2016	346	2016
17	11145	A6	443	2017

most samples variously sized black magnetite crystals are embedded, and every sample contains – in various quantities – differently sized iron droplets. The inside of the vesicles is usually a blackish, frequently glassy "nest" with metal globules.

The surface of samples 2318, 2340, 4169, 4222 and 4251 is also heterogeneous, but (excepting 2318 with a clayish core) are dark grey or blackish inside. The structure is denser, assuring a greater hardness, so pulverisation is usually difficult. Sample 4137 is sandwich-structured: a 3-4 mm thick terracotta outer layer which covers a 3-4 mm thick black inner layer, which in turn covers a terracotta core.

Macroscopic morphology of the samples unearthed at the principia show some differences when compared to the vicus samples. The relatively dense, stratified 10218 contains plenty of small vesicles. The outer clayish layer is pulverulent, the vitrified core being blackish, with many small metallic globules; so its fracturation and trituration is difficult.The dark grey sample 10532 is compact, with large glassy vesicles nesting

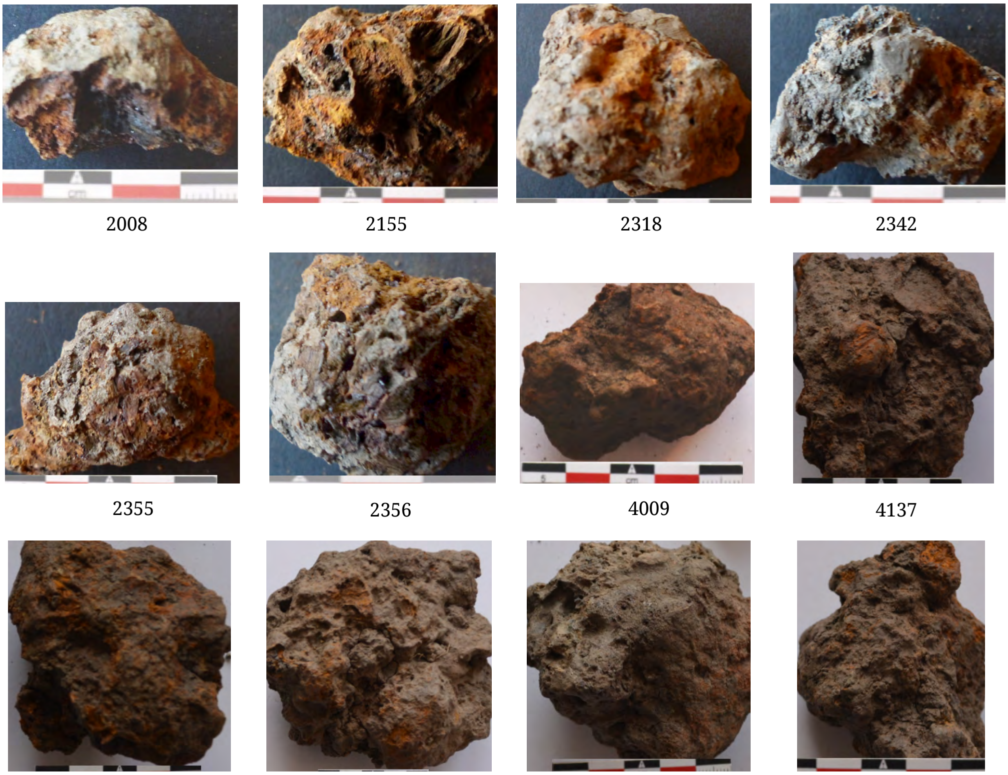

2008 2155 2318 2342

2355 2356 4009 4137

4169 4222 4251 4264

Figure 3. *Macrophotos of the samples finds from the vicus*


10218 10532 10661 10673 11145

Figure 4. *Macrophotos of the samples finds from the principia*

many iron "beads". It is brittle, but its grinding is difficult. The compact 10661 is even harder, but is fissile (easily splits into layers). The surface is grey, the inside is clayish red and with some small iron globules in the blackish cracks. The lighter, spongy, moderately blistered 10673 and 11145 are susceptible to lamellary-columnal fracturation and can be easily ground. Their surface is greyish-red, their core is reddish-clay, lamellary structured, with some white crystalline material, larger magnetite crystals and iron inclusions.

2.2. Investigation methods and results

2.2.1. Optical microscopy (OM)

The microphotos **[5, 6]** were obtained at 500x magnification on the raw outer surface, and the fresh, rough (unpolished) core surface (cleavage) obtained by crushing the samples, were registered using a Dino-Lite Edge AM4115T digital microscope without polarisation and the DinoCapture 2.0 image processing software. Some of the most characteristic microphotos are presented on the **Figures 5.** és **6.**

The mineralogical interpretation of the OM data obtained (the identification of the mineral components) is in progress, however, some general characteristics of the samples can be concluded.

The totality of the samples contain, in different quantities, differently sized gas lunkers and iron inclusions (metallic droplets separated typically in the inside of the gas holes or in the cracks where they were formed). Additionally, cubic magnetite crystal inclusions appear in every sample, although they are fewer. **[7]**

2.2.2. FTIR spectroscopy

FTIR spectra of the archaeological finds can be used as a convenient tool for the elucidation of the chemical processes that occured during their genesis (fabrication or simply formation as in the case of the iron slags), and the geochemical (alteration) processes taking place during their burial **[8–10]**. In the case of the archaeological iron slags, the wide, tipycally medium intensity absorption bands appearing in the 3700-3000 cm^{-1} spectral region, generated by free and (physically or chemically) bonded OH, together with the

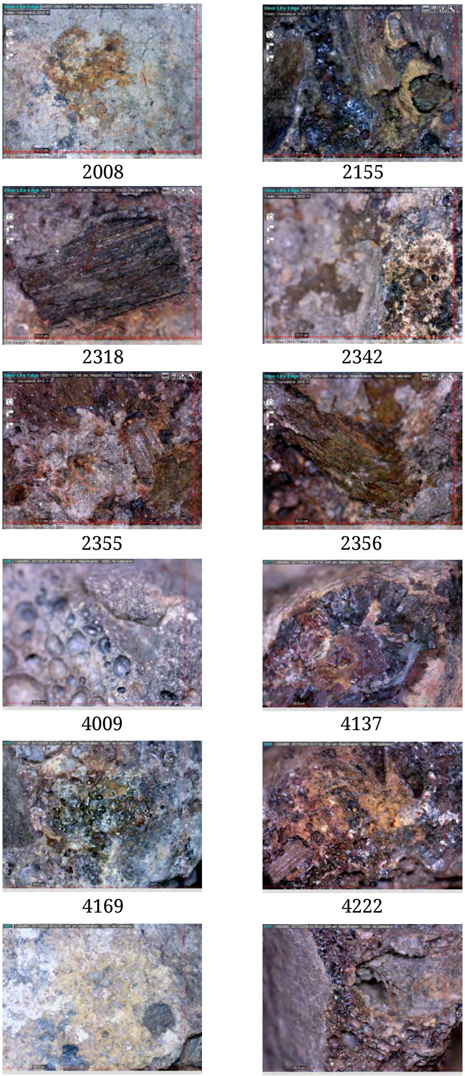
2008 2155
2318 2342
2355 2356
4009 4137
4169 4222
4251 4264

Figure 5. *Selected microphotos of the vicus samples (500x)*

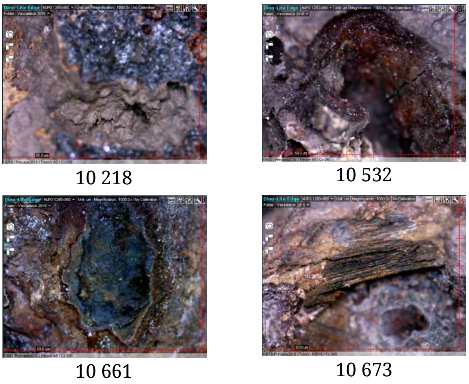
10 218 10 532
10 661 10 673

Figure 6. *Microphotos obtained on principia samples (500x)*

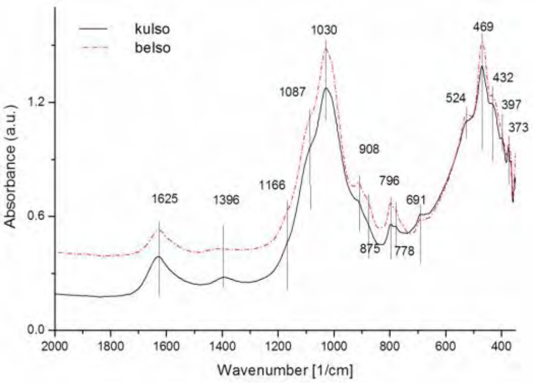

Figure 7. *FTIR spectrum of the iron slag surface layer (black) vs. the inside material (red); sample 4009*

wide, intense, quasi-symmetrical (alumino)silicate bands shown between 1100-1000 cm^{-1}, reliably characterize the structural order (or disorder) of the samples. Structural ordering of the iron slags is the result of the crystallization that occurred during the cooling of the melted material, followed by the metamorphosis (alteration) processes occurring during burial, the latter largely depending on the local environmental particularities of the archaeological site. The spectral components identified by means of the spectral deconvolution of the above mentioned main absorption bands can confirm (reinforce) the mineralogical componency resulting from the petrographic microscopy, XRD and macroelemental analysis data of the samples.

The FTIR absorption spectra in the 4000-400 cm^{-1} region were obtained on KBr pellets of the agate mortar pulverised samples without any kind of prior thermal treatment. The spectra were recorded using a JASCO FTIR 6100 spectrometer of 1 cm^{-1} resolution. The composition of the pulverised samples was, as far as possible, close to the homogenized bulk composition. FTIR spectra on the surface layer and the inside of the 4009 sample in the 2000-400. cm^{-1} region were also recorded (**Figure 7.**)

Due to the absence of deconvolution data in relation to the major OH absorption band, an adequate interpretation of the 4000-2000 cm^{-1} spectral region is uncertain, assignation of the main absorption peaks was made in the 2000-400 cm^{-1} region (**Table 2.** presents the data obtained for the vicus samples 4009-4264).

As an exception, in case of three selected samples that presented a peculiar archaeological interest (the 2155, from the vicus, and the 10218 and 10532, from the principia), the peak assignation was extended to the whole spectrum (**Figure 8.**, **Table 3.**).

Table 2. *Assignments of the FTIR absorption peaks (bulk) in the 2000-400 cm^{-1} region*

Wavenumbers (cm^{-1})						Assignments*
4009	**4137**	**4169**	**4222**	**4251**	**4264**	
1630	1620	1625	1620	1627	1630	OH, FeO(OH)
1394 sh	1698	1396	1396	1394	1401	CO_2
1167 sh 1076 sh 1045	1084 sh 1029	1166 sh 1087 sh 1030	1166 sh 1087 sh 1030	1094 sh 1025	1165 sh 1080 sh 1023	SiO_4, AlO_4 dominant mode FeO(OH) 1084
913 876	882	908 875	908 875	906 sh	913 sh	Fe_2O_3 1100 CO_2 880-860
794 776	796 779	796 778	796 778	798	796 778	SiO_4, AlO_4 dominant mode FeO(OH) 803
524 462 421	526 467 435	524 469 462 sh	524 469 462 sh	524 sh 467 428	526 sh 471 421	Fe_2O_3 550, 417 FeO(OH) 470, 410 Si-O, Al-O, 470-460

* Based on the RRUFF database

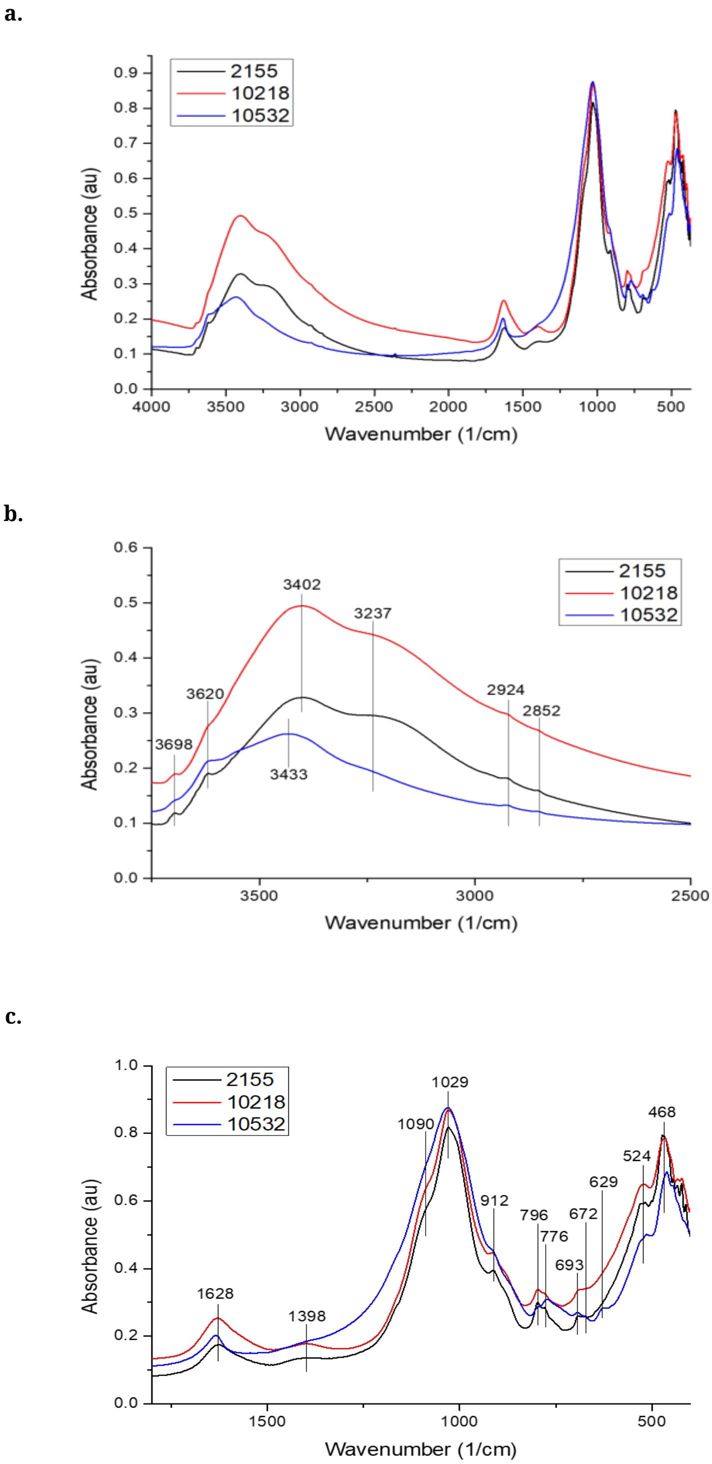

Figure 8. *FTIR spectra of three iron slags selected for detailed characterization: (a) 4000–400 cm^{-1}, (b) 4000–2500 cm^{-1}, (c) 2000–400 cm^{-1}*

Table 3. *FTIR data of the three selected samples in the 4000-400 cm^{-1} region*

Wavenumbers (cm^{-1})			Assignments*
2155	10218	10532	
3618	3621	3616	OH
		3549	
3401	3403		
3221	3220	3243	
2923	2924	2914	
2853	2851	2854	
1627	1629	1635	
1398	1398	1393	SiO_4
1090	1090		SiO_4, AlO_4 1100-900 FeO(OH), Fe_2O_3 1105, 1084
1029	1030	1030	
912	915	914	
797	797	799	SiO_4 798-782, FeO(OH) 803
779	777	773	FeO(OH)
693	695	693	AlO_4
		627	SiO_4 630
520	523	515	Fe_2O_3
471	465	431	FeO(OH) 470 Fe_2O_3 432

According to **Figure 7.**, in the case of sample 4009, the FTIR spectra corresponding to the outer layer and the inside of the sample in the 2000-400 cm^{-1} region practically coincide. This indicates that even if some geochemical processes took place during burial, their influence, at least in this case, is negligible. Corroborating this with the **Table 2.** data (which indicate a parallelism of the spectral behaviour of the different samples), it is probable that in most cases the FTIR study carried out on probes corresponding to the bulky composition of the samples is good enough.

Comparing the absorption peak assignments presented in the **Table 2.** and **3.** indicates that the FTIR spectroscopic behaviour of the two sample groups (from the vicus and the principia), at least in the region 2000-400 cm^{-1}, is also similar, even if some minor differences can be observed. So far, in case of the Călugăreni site, the FTIR spectroscopic behaviour of the slag samples does not depend on the exact location where they were unearthed. However, this conclusion (or further conclusions) needs more data obtained by further methods, such as the actual ongoing XRD, XRF, ICPMS investigations.

3. Conclusions

The Roman auxiliary fort located at Călugăreni, on the Eastern sector of the Dacian *limes*, established after the Roman conquest of the Dacian kingdom, was a strategically important military centre. During the still ongoing archaeological excavations a large quantity of iron slag remains have been unearthed. However, to date, no trace of bloomery or smithery workshops was found at the location. In consequence, the source of the slag finds is unknown; they could originate equally from the local processing of some imported iron blooms, or from the recovery of damaged iron objects (weapons and household tools) by reparation or recycling. The issue could be clarified to some extent by means of the archaeometric study of the slag finds. In this case, the thorough investigation of 17 carefully selected iron slag samples was initiated. In this first stage, after a macroscopic evaluation of the morphology, optical microscopy and FTIR spectroscopy was carried out on the specimens.

According to the characteristic FTIR absorption peaks appearing in the spectral domain 2000-400 cm^{-1}, the investigated samples among some carbonates (and possibly aluminates) are constituted from silicates. The carbonates could have been formed in carbonation processes taking place during burial, as a consequence of the environmental conditions.

According to the microphotos registered, the main crystal phase of the samples identified in the absence of polarized light is fayalite (Fe_2SiO_4); dendritic wüstite and cubic magnetite are also observed in practically every sample. The samples generally are characterized by a vast amount of metallic iron inclusions, and the presence of some glassy phases. These considerations indicate that the (smelting or smithy) processes the samples were subjected to took place at relatively high temperatures, probably in a reducing atmosphere or environment.

According to the macroscopic characteristics, the possibility that the slags could be smelting by-products can't be excluded. The morphology of some samples are close to that of the tap slags: these specimens are more dense, with small blow holes inside, as the tap slag froze outside the smelter. The lower density, sponge-like structured samples full of gas lunkers seem to have been cooled down inside the smelter (cinder).

In future, research will continue with petrographic microscopic and XRD investigation, and macro- and microelemental analysis of the samples. Naturally, we have to keep in mind that (as indicated by the standard deviation values associated with the previous PXRF elemental analyses of the surface composition of similar samples) these types of sample are very heterogeneous. [11, 12]. In consequence, conclusions referring to the slag's mineralogical and/or chemical composition have to be drawn very cautiously.

Acknowledgement

The archaeometric (archaeometallurgical) research carried out is part of the *Project for Technical and Cultural Heritage Preservation in Transylvania*, initiated and supervised by the Research Institute of the Transylvanian Museum Society. The financial support was assured by the 3272/4/2017/HTMT grant of the Homeland Research Programme supervised by the Hungarian Science Abroad Presidential Committee of the Hungarian Scientific Academy.

The field research between 2013-2015 was organized as the archaeological field school of the international interdisciplinary project *The Roman Limes as a European Cultural Landscape* coordinated by: the Mureş County Museum and the Winckelman Institute of the Humboldt University of Berlin. The field school involved the participation and cooperation of students and lecturers of archaeology, geophysics, architecture, conservation and restoration from the University of Cologne, the University of Pécs, the Budapest University of Technology and Economics, the Eötvös Loránd University, the University of Applied Sciences Erfurt, the Babeş–Bolyai University of Cluj-Napoca, and the Petru Maior University of Târgu Mureş.

Since 2016, the archaeological research was supported by the Mureş County Council, the Chair of the Roman Provinces at the Archaeological Institute of the University of Cologne, the Erasmus Fund of the Humboldt University of Berlin, and the Romanian Ministry of Culture.

References

[1] Matei-Popescu F., Ţentea O.: *The Eastern Frontier of Dacia. A Gazetteer of the Forts and Units*. In: Orbis Romanus and Barbaricum. The Barbarians around the Province of Dacia and Their Relations with the Roman Empire. (Ed.: Bârcă V.). Mega Publishing House, Cluj-Napoca, 2016. 7–24.

[2] Höpken C. et al.: *Wachtürme am Dakischen Ostlimes zwischen Brâncoveneşti und Călugăreni (jud. Mureş/RO)*. Archäologisches Korrespondenzblatt 46. (2016) 241–254.

[3] Pánczél Sz. P.: *The Roman Fort from Călugăreni (Mureş County, Romania)*. In: LIMES XXII. Proceedings of the 22nd International Congress of Roman Frontier Studies Ruse, Bulgaria, September 2012. (Eds.: Vagalinski L., Sharankov N.). National Archaeological Institute with Museum, Sofia, 2015. 909–916.

[4] Pánczél Sz. P. et al.: *A mikházi római segédcsapattábor kutatása/The research at the Roman auxiliary fort of Mikháza/Călugăreni*. Magyar Régészet/ Hungarian Archaeology, 2018 spring, 13–20. http://files.archaeolingua.hu/2018TA/Pa%b4ncze%b4l_E18TA.pdf

[5] Buchwald V. F., Wivel H.: *Slag analysis as a method for the characterization and provenancing of ancient iron objects*. Materials Characterization, 40. (1998) 73–96. https://doi.org/10.1016/S1044-5803(97)00105-8

[6] Kramar S. et al.: *Mineralogical and geochemical characterization of Roman slag from the archaeological site near Mosnje (Slovenia)*. Materials and technology, 49. (2015) 343–348. http://mit.imt.si/Revija/izvodi/mit153/kramar.pdf

[7] Mihailova I., Mehandjiev D.: *Characterization of fayalite from copper slags*. Journal of the University of Chemical Technology and Metallurgy 45. (2010) 317–326. http://dl.uctm.edu/journal/node/j2010-3/12_Irena_Mihailova_317-326.pdf

[8] Sowmya T., Sankaranarayanan S. R.: *Spectroscopic analysis of slags – preliminary observations*. In: VII. International Conference on Molten Slags, Fluxes and Salts, The South African Institute of Mining and Metallurgy, South Africa, 2004. 693–697. http://www.saimm.co.za/Conferences/MoltenSlags2004/693-Sowmya.pdf

[9] Olovčić A., Memić M, Žero S, Huremović J., Kahrović E.: *Chemical Analysis of Iron Slags and Metallic Artefacts from Early Iron Age*. International Research Journal of Pure and Applied Chemistry, 4. (2014) 859–870. https://doi.org/10.9734/IRJPAC/2014/12248

[10] Sheikh M. R. et al.: *Characterization of iron slag of Kakching, Manipur by X-ray and optical spectroscopy*. Indian Journal of Pure & Applied Physic, 48. (2010) 632–634. http://nopr.niscair.res.in/bitstream/123456789/10153/1/IJPAP%2048%289%29%20632-634.pdf

[11] Chuenpee T., Won-In K., Natapintu S. Takashima I.: *Archaeometallurgical Studies of Ancient Iron Smelting Slags from Ban Khao Din Tai Archaeological Site, Northeastern Thailand*. Journal of Applied Sciences, 14. (2014) 938–943. https://doi.org/10.3923/jas.2014.938.943

[12] Scott R. B. Eekelers K., Degryse P.: *Quantitative chemical analysis of archaeological slag material using handheld X-ray fluorescence spectrometry*. Applied spectroscopy, 70. (2016) 94–109. https://doi.org/10.1177/0003702815616741

Acta Materialia Transylvanica 1/2. (2018) 73–76.
https://doi.org/10.2478/amt-2018-0024
Hungarian: ~~https://doi.org/10.2478/amt-2018-0023~~
https://doi.org/10.33923/amt-2018-0023
Corrected: 29.08.2023.

Analysis of Recrystallization Peak Occuring During DSC Measurement

Gergő Richárd FEJES[1], Viktor GONDA[2], Károly SZÉLL[3]

[1, 2] *Óbuda University, Donát Bánki Faculty of Mechanical and Safety Engineering, Institute of Materials and Manufacturing Sciences, Department of Materials Technology, Budapest, Hungary*

[1] *fejesgergorichard@gmail.com;* [2] *gonda.viktor@bgk.uni-obuda.hu*

[3] *Óbuda University, Alba Regia Mechanical Faculty, Székesfehérvár, Hungary*

Abstract

Severe plastic deformation (SPD) is a well-established methodology for the processing of bulk ultrafine grained materials. Among various methods, equal channel angular pressing (ECAP) is the most popular way of creating ultrafine grained materials. The stored energy after ECAP in these substances highly influences the microstructural processes: recovery and recrystallization of the processed materials. We analyzed the recrystallization kinetics of room and elevated temperature ECAP processed copper samples using differential scanning calorimetry (DSC). For the processing of the measurement data we developed a MATLAB processing routine.

Keywords: *ECAP, DSC, MATLAB, recrystallization, copper.*

1. Introduction

Equal channel angular pressing (ECAP) is one of the severe plastic deformation (SPD) methods, by which grain refinement can be achieved in cold working, and bulk ultrafine grain materials can be produced. The large deformation induced during ECAP results in microstructural alterations. Grains are distorted and textured, dislocation density increases and saturates within the grains. Subsequently, dislocations pile up, and arrange in walls, thereby subgrains are formed and grain refinement occurs. Part of the energy introduced by the deformation is stored in the material in the dislocations; this energy is released by recrystallization and also acts as a driving force for recrystallization. This stored energy highly influences all kinds of microstructural transformations. In the present work – as a follow up to a prior study [1] -, ECAP was performed on electrolyte copper specimens at room temperature and at elevated temperatures. Thermal behaviour of the deformed samples was then examined by annealing in differential scanning calorimetry (DSC) equipment. During annealing, an exothermal peak arises at recrystallization in the DSC heat flux data, namely a recrystallization peak, which can be related to the stored energy released by the transformation. Prior to this, we analyzed manual processing methods of the peak to extract results. In the present work, we show results for recrystallization of ECAP processed samples at elevated temperatures, where the results were obtained by an automated data processing procedure of the DSC data created in MATLAB.

2. Experimental procedures

2.1. Equal Channel Angular Pressing (ECAP)

The material for ECAP processing was commercially available pure electrolyte copper in the form of extruded rods. Specimens were machined to a diameter of 10 mm and a length of 60 mm. Prior to ECAP, specimens were annealed at 450°C for 1 hour.

ECAP processing was performed at several temperatures: room temperature, 50, 100, 150, and 200°C, with a feed of 8 mm/min in an ECAP die with 110° channel angle. Specimens were single pass processed, pressing forces were recorded during the deformations. To reduce friction, Molykote grease was employed, which is applicable from –30°C to 1100°C temperature range.

After the deformations, at least 4 coin shaped samples were machined from each specimen for DSC, with a geometry of ϕ5,9×2,5 (mm) or ϕ5,9×1 (mm).

2.2. Differential Scanning Calorimetry (DSC)

For the thermal analysis, a Perkin-Elmer power compensated DSC-8000 was employed. In this equipment the heating power for linear heating of a specimen is controlled with a thermally neutral reference sample. The measured quantity is the power difference that is required for heating of the measurement and reference samples, and which can be plotted as a function of the temperature of time.

Annealing experiments were performed for the samples obtained at ECAP processing at room temperature, 50, 100, 150, and 200°C. Heating rates in the DSC measurements were 5, 10, 20, and 50°C/min.

Samples were heated from room temperature to above the recrystallization temperatures, so that the transformation completed, in the first samples up to 400°C, later based on the experiences up to 350°C. Heat flux was recorded by the control software of the equipment, called Pyris, and the sampling rate was set to obtain about 10000 data points for each measurement. A set of measurement results is illustrated in **Figure 1.**

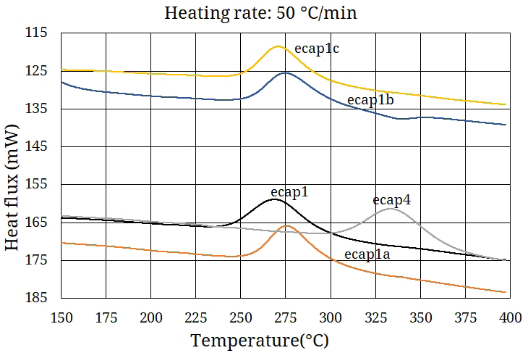

Figure 1. *Heat flux recorded by DSC at a heating rate of 50°C/min for the ECAP processed samples at different temperatures*

3. Data processing

Due to the large number of recorded data points, an automated processing routine was required. The developed MATLAB processing routine requires minimal user interaction and provides quick, reliable results. Previously, we manually processed DSC data with the Pyris software, and also with the help Origin and Excel. We validated results obtained by the MATLAB routine with the manually processed data.

The MATLAB routine is controlled by a list of DSC data filenames, sample masses, and heat rates. These data are loaded into an array, then each data file in the list is processed. During the first stage of processing, the DSC data file is loaded, the measured data is plotted. Here, the program requires user interaction on the graphical interface, to point the onset and the end of the recrystallization peak. Then, the base line is determined by a 3rd order polynomial fitting, the goodness of fit can be visually inspected, and then the measurement data compensated by subtracting the base line. All properties of the peak are calculated subsequently and the results (to 3-digit precision) are stored in the tab separated text file. The resulting file contains: name of data, mass, heating rate, peak temperature, specific stored energy, and peak height. After the results are stored, a figure is created by a subroutine, plotting the compensated peak in a subtracted specific heat flow versus the temperature diagram, and labels the diagram with the most important calculated results (peak temperature, peak height, area under the peak – stored energy) (**Figure 2.**). For each dataset, such figure is plotted and stored.

In the present dataset, each ECAP processing, contains four DSC samples. For this set, a processing routine generates a summary plot after four peaks are processed, from which differences due to the heating rates can be analyzed. This is then used for the determination of the activation energies of recrystallization.

Moreover, the program generates a figure about the fitted polynomial, the kinetics of the transformation as a function of the temperature. A detailed description of the program and its source code is available in [2].

The activation energy for recrystallization was calculated by the Kissinger theory [3].

4. Results

The analysis of the results of the processed DSC data for each of the ECAP processing temperatures helps to understand the thermal behavior of the highly deformed materials. To illustrate the analysis, we selected the results for the 5°C/min heating rates from the measurement set.

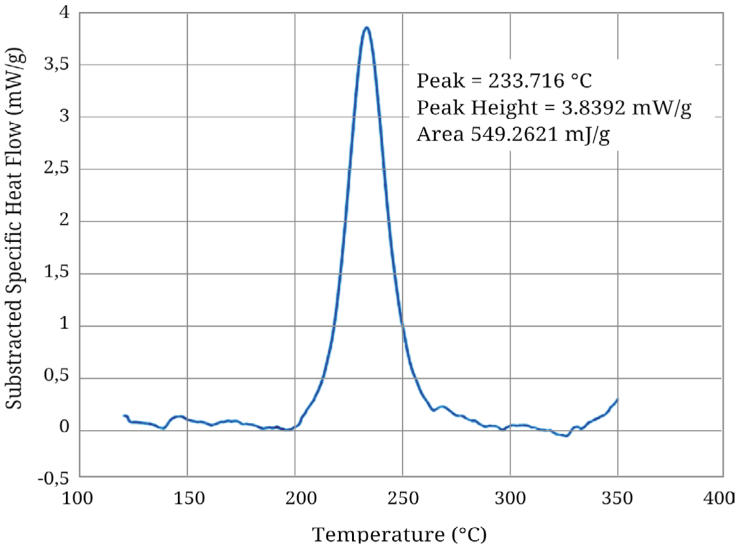

Figure 2. *A plot of the compensated recrystalliza-tion peak with labels of the calculated peak properties*

The peak temperatures, as a function of the ECAP processing temperature, is shown in **Figure 3.** It can be seen that the exothermic peak temperature, which marks the recrystallization transformation, steadily increases in the examined processing temperature range.

We can conclude by this observation that the increase in the deformation temperature - the energy required for initiating the recrystallization - also increases for the samples in different states.

The stored energy in the samples is released by recrystallization, the magnitudes are shown as a function of the ECAP processing temperature in **Figure 4.** The decrease in the stored energy shows that by increasing the processing temperature, less energy is stored in the dislocations of the material.

The effect of the heating rates on a sample in a given state can be shown in the Arrhenius-plots, by which the activation energy can be determined. The variation of the activation energies as a function of the ECAP processing temperatures are shown in **Figure 5.**

By analyzing the activation energies, we can conclude that the activation energy is the lower at about 86 kJ/mol at room temperature ECAP processing. The stored energy in the material was the highest in this case. With increasing processing temperature, as expected by the increasing peak temperatures and decreasing stored energies, activation energies increase slightly.

Based on these results we can conclude that the by increasing the ECAP processing temperature, the applied deformation energy is also lower, some transformation might already have occurred

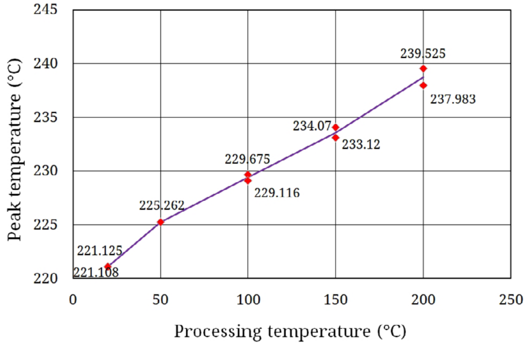

Figure 3. *Recrystallization peak temperature as a function of the ECAP processing temperature.*

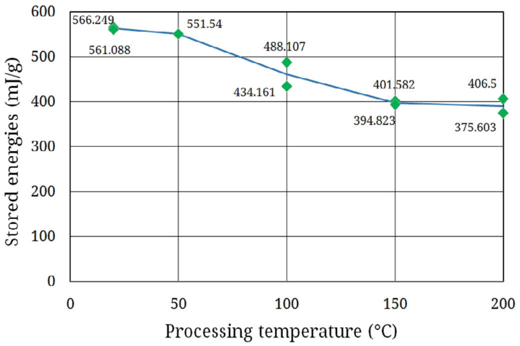

Figure 4. *Stored energies as a function of the ECAP processing temperatures*

during the processing, the onset is delayed for recrystallization transformation, stored energy is decreased, and activation energy is slightly increased.

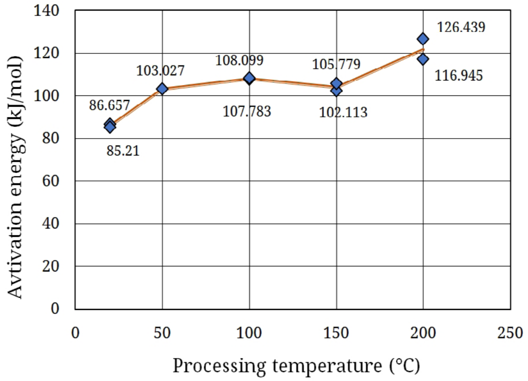

Figure 5. *Activation energies as a function of the ECAP processing temperatures*

Acknowledgement

This research was supported by EFOP-3.6.1-16-2016-00010.

References

[1] Fejes G. R., Gonda V.: *Könyöksajtolt réz próbatestek DSC vizsgálata.* In: A XXII. Fiatal műszakiak tudományos ülésszaka előadásai. Proceedings of the 22th international scientific conference of youngth engineers, Cluj-Napoca, Romania, Műszaki Tudományos Közlemények 7. 2017. 151–154. https://eda.eme.ro/handle/10598/29768

[2] Fejes G. R.: *Könyöksajtolt réz próbatestek DSC vizsgálata.* In: XLV. Tudományos Diákköri Konferencia, Óbuda University, Budapest, 2017.

[3] Benchabane G., Boumerzoug Z., Thibon I., Gloriant T.: *Recrystallization of pure copper investigated by calorimetry and microhardness*. Materials Characterization, 59/10. (2008) 1425–1428. https://doi.org/10.1016/j.matchar.2008.01.002

Acta Materialia Transylvanica 1/2. (2018) 77–80.
https://doi.org/10.2478/amt-2018-0026
Hungarian: ~~https://doi.org/10.2478/amt-2018-0025~~
https://doi.org/10.33923/amt-2018-0025
Corrected: 29.08.2023.

Thermographic Inspection in the Electric Industry

Ferenc HARASZTI

Óbuda University, Donát Bánki Faculty of Mechanical and Safety Engineering, Institute of Materials and Manufacturing Sciences, Department of Materials Technology, Budapest, Hungary
haraszti.ferenc@bgk.uni-obuda.hu

Abstract

The traditional inspection of fittings used in the electrical industry is a cumbersome, dangerous process in terms of safety and operation. However, with the spread of thermography, these tests can be performed simpler, faster, and more safely through electrical connections. This article presents the possibilities, measurement difficulties and the advantages of thermography analysis [1-2].

Keywords: *thermography, thermographic camera, electrical industry.*

1. Introduction

There are a large number of electrical fittings in the electricity industry. Most of which utilize copper, steel, aluminium and their alloys [3–8]. Due to differences in the potential of different materials, galvanic corrosion may occur. This process can lead to failure of the joint. The increased resistance causes heat generation is shown in Figure 1. and Figure 2.

Therefore, we have used a thermal imaging procedure over the past few years. The benefits include safe and uninterrupted measurement. Previously we investigated the relationship between heat development and current.

Our measurements could only be accurate within a certain tolerance as metals can change their electrical resistance due to heat, which can only result in thermal evolution according to the degree of heating. In this paper, we test copper and steel used in the electrical industry. The copper-steel coupling resistance varies as a function of the temperature.

1.1. Resistance to the temperature dependence

If a metal is subjected to a strong heating effect, its resistance increases. It can be stated that the resistance generally depends on the temperature [9, 10]. For metals, the temperature increases proportionally, with semiconductors, coal, and electrolytes proportionally decreasing. Examined at extremely high temperatures and relatively small intervals, the specific resistance ρ of the

Figure 1. *Galvanic corrosion affected damage*

Figure 2. *Galvanic corrosion affected damage*

metals in question is proportional to the temperature range tested **[11]**.

The applied relationship *(1)*:

$$\frac{\rho-\rho_0}{\rho_0} = \propto (t-t_0) \qquad (1)$$

where:

ρ = specific resistance (Ωm),
α = temperature coefficient (1/C°),
t = temperature (C°).

Instead of the specific resistance, we can use the concept of equivalent electrical resistance, and then our relationship is as follows *(2)*:

$$R = R_{20}\,(1 + \alpha_{20} \cdot \Delta t) \qquad (2)$$

where:

R = electrical resistance (Ω),
R_{20} = Resistance on 20 C° (Ω),
α_{20}= Temperature factor on 20 C° (1/C°).

The resistivity of the copper and steel fittings used in industry as a function of temperature is shown in the graph below (**Figure 3.**).

In our case, it is not necessary to extend the temperature range (0-700 °C), as the harmful warming of the abnormally fast electrical binder can be done in this interval.

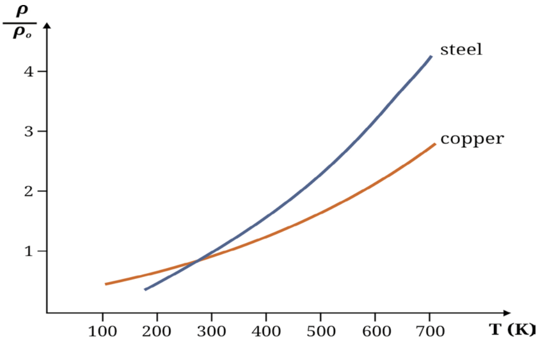

Figure 3. *Resistance versus temperature [6]*

1.2. Non-contact temperature measurement

The infrared-based temperature measurement and thermal imaging method depend on the heat radiating ability of the bodies. Temperature radiation is the process that emits electromagnetic waves due to heat movement in the material. Much of this energy can be emitted or reflected on another body and can be transmitted. If radiation arriving on the test body is absorbed without any remaining excess heat, then we are dealing with an absolutely black body.

In practice, we use the laws of physics. The infrared range of the electromagnetic spectrum emitted by the surface of the object under consideration is measured with the thermal camera and transformed into an electric signal **[6-7]**. The accuracy of our measurement data is mainly determined by the instrument specification itself, the medium of the object to be measured and the surface of the object to be measured. The wavelength of the light we perceive varies between 0.4 and 0.75 μm. The infrared range may differ from this range between 0.75 and 20 μm. In heat detector analysis practice, we can examine this range.

2. Examination of electrical fittings

Our goal is to determine the resistance of a steel-copper pair depending on the temperature. How much does it contribute to the electrical resistance of a steel-copper connection with high contact resistance with galvanic corrosion? What degree of resistance is represented by the general electrical contact used in the industry when considering only the parameters examined by warming?

On the base of the literature data, the specific resistance (and R resistance) is not significantly considerable about the view of the temperature. Nevertheless, it is important to know how its values develop if we are not testing it under laboratory conditions. In our case, an everyday copper rack and a steel screw are the subjects of the test (**Figure 4.**).

The measurement is performed in the assembled condition, tightening the screw with the correct torque. Due to the magnitude and accuracy of the resistance value, we work with a Wheatstone bridge measurement method. The applied thermal imaging camera ensures contactless temperature reading without interruption **[12]**. The heating of the electric joint component is supported by a precision electrical heater. The schematic diagram of the measurement is shown in **Figure 5.** and the setup of the measurement is shown in **Figure 6.**

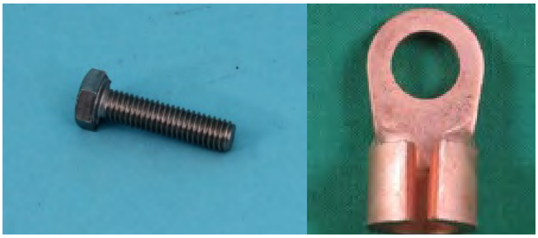

Figure 4. *Fittings*

2.1 Measurement results

During the experiment, five series of measurements were prepared and after error calculation, the following results were obtained (**Table 1.**):

The resultsof resistence as a function of the temperature, shown in the next diagram (**Figure 7.**) .

By evaluating this, we can conclude that the course of the function is similar to pure conductive materials of high precision, accredited laboratory conditions, showing linearity.

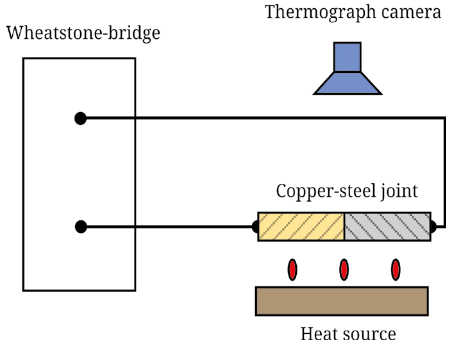

Figure 5. *Schematic diagram of the measurement*

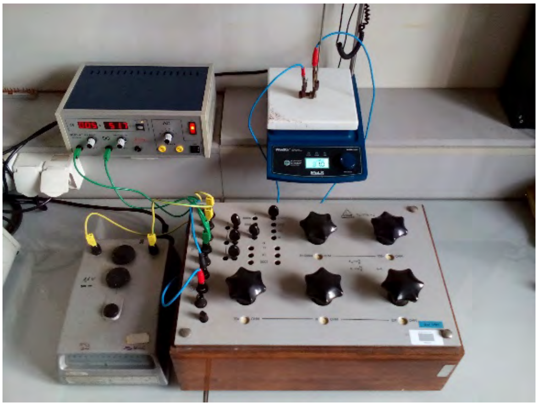

Figure 6. *Setup of the measurement*

Table 1. *Measured values*

Number	Temperature C°	Resistance Ω
1.	254	0.1
2.	309	0.2
3.	360	0.3
4.	410	0.4
5.	460	0.5
6.	505	0.6

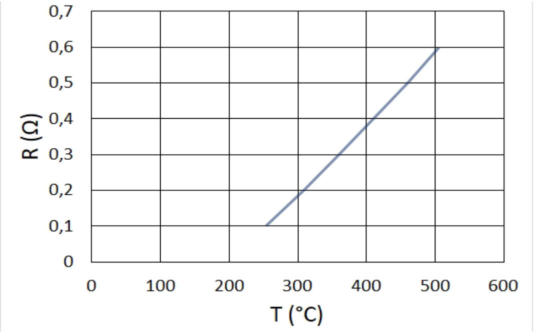

Figure 7. *Resistance ratio temperature dependence*

3. Conclusions

The aim of our study was to examine the resistance of the current-conducting components used by the electrical industry as a function of temperature. Is it different and, if so, how much does it deviate from the literature values? The difficulty of the measurements and the accuracy of the evaluation were given by the differences in production, given that a multimember assembly was the subject of the test. Comparing the temperature factors for each material found in the literature with the copper-steel component we find the following:

The copper and steel temperature coefficient varies between $\alpha_{20} = 3{,}92 \cdot 10^{-3}$ and $4{,}2 \cdot 10^{-3}$. During our measurement, we have shown a multiple or even a magnitude increase of 250 °C to 500 °C (30 – $40 \cdot 10^{-3}$). EAt these temperatures, therefore, one piece of one Ohm resistive material changes its value by 1 °C. The resistance of the electric fittings exposed to the aforementioned contact corrosion is therefore not only increased by the increase of the transition resistance. We must also account for the increase in the resistance of the material in this way, especially if it is necessary to accurately keep the temperature characteristics of a component: according to the results of this paper, depending on the current, several different 10 °C differences may occur. Other factors influencing the resistance may also include mechanical (pressure and stretching) of electrical components.

References

[1] Haraszti F. : *The bases of corrosion's investigation.* In: Proceedings of the 21th international scientific conference of youngth engineers, Cluj-Napoca, Romania, Műszaki Tudományos Közlemények 5. (2016) 185–188. https://eda.eme.ro/handle/10598/29058

[2] Haraszti F.: *Corrosion investigation of steel samples*. In: Proceedings of the 21th international sci-

entific conference of youngth engineers, Cluj-Napoca, Romania, Műszaki Tudományos Közlemények 5. (2016) 189–192.
https://eda.eme.ro/handle/10598/29057

[3] Kovács-C. T., Völgyi B., Sikari-Nágl I.: *Galvanic corrosion behaviour testing in case of aluminium and steel couple*. In: Fiatal műszakiak tudományos ülésszaka XVIII., Cluj-Napoca, Romania, Műszaki Tudományos Füzetek 2013. 201–204.
https://eda.eme.ro/handle/10598/26880

[4] Kovács-C. T., Völgyi B., Sikari-Nágl I.: *Investigation of aluminium-steel joint formed by explosion welding*. Journal of Physics – Conference Series 602. (2015) 1–4.
https://doi.org/10.1088/1742-6596/602/1/012026

[5] Wu Y., Barton S. C., Lee A.: *Galvanic corrosion behavior at the Cu-Al ball bond interface: Influence of Pd addition and chloride concentration*. Microelectronics Reliability, 92. (2019) 79–86.
https://doi.org/10.1016/j.microrel.2018.11.016

[6] Hack H. P.: *Galvanic Corrosion*. Reference Module in Materials Science and Materials Engineering, 2016.
https://doi.org/10.1016/B978-0-12-803581-8.01594-0

[7] Hakansson E., Hoffman J., Predecki P., Kumosa M.: *The role of corrosion product deposition in galvanic corrosion of aluminum/carbon systems*. Corrosion Science, 114. (2017) 10–16.
https://doi.org/10.1016/j.corsci.2016.10.011

[8] Khadom A. A., Abod B. M.: *Mathematical model for galvanic corrosion of steel-copper couple in petroleum waste in presence of friendly corrosion inhibitor*. Journal of Applied Research and Technology, 15. (2017) 14–20.
https://doi.org/10.1016/j.jart.2016.10.004

[9] Wellons M.: *The Stefan-Boltzmann Law*. Physics Department, College of Wooster, Wooster, Ohio 44691, USA, May 9, 2007.
http://g.wooster.edu/JrIS/Files/Wellons_Web_Article.pdf

[10] Dománková M., Kocsisová E., Slatkovský I., Pinke P.: *The Microstructure Evolution and Its Effect on Corrosion Properties of 18Cr-12Ni-2,5Mo Steel Annealed at 500-900°C*. Acta Polytechnica Hungarica, 11/3. (2014) 125–137.
https://www.doi.org/10.12700/APH.11.03.2014.03.8

[11] Kittel C., Kroemer H.: *Thermal Physics ASTM Standard Practice in A 262 for Detecting Susceptibility to Intergranular Corrosion in Austenitic Stainless Steels*. W. H. Freeman and Company, 1980.

[12] Budó Á.: *Kísérleti Fizika II*. Tankönyvkiadó, Budapest, 1971.

Acta Materialia Transylvanica 1/2. (2018) 81–84.
https://doi.org/10.2478/amt-2018-0028
Hungarian: ~~https://doi.org/10.2478/amt-2018-0027~~
https://doi.org/10.33923/amt-2018-0027
Corrected: 29.08.2023.

Corrosion Testing of Additively Manufactured Metals and Biomedical Devices

Dávid Miklós KEMÉNY[1], Dóra KÁROLY[2]

Budapest University of Technology and Economics, Faculty of Mechanical Engineering, Department of Materials Science and Technology, Budapest, Hungary

[1] kemenydavid@edu.bme.hu

[2] kdora@eik.bme.hu

Abstract

Additive manufacturing (AM) is becoming increasingly important, making it possible to produce a product in a short time, to specific individual requirements, and even in the presence of the customer. This research is related to direct metal laser sintering of additive manufacturing. This new technology is increasingly being used in more sectors, for example in biomedical industry, where a damaged product can potentially endanger human life. Corrosion tests were carried out during our research. Cyclic voltammetry curves and corrosion rates were determined with a potentiostat. Two typical biocompatible implant materials were compared, a cobalt chromium alloy (powder metallurgy) and a titanium alloy (3D printed). The results will help in specifying the corrosion properties of additively manufactured materials.

Keywords: *additive manufacturing, direct metal laser sintering, corrosion, cyclic voltammetry*

1. Introduction

Nowadays, the use of additive manufacturing technologies is becoming more widespread. For this reason, complicated products can now be made precisely and quickly, even in the presence of the customer. With this technology, three-dimensional bodies can be created which are not possible or are too difficult to produce with conventional technology. This process was initially used with polymers, but today it can be applied to almost all raw materials: metals, plastics, ceramics, papers or a combination of these (composites) **[1, 2]**.

Before additive manufacturing, a 3D model is required, which is produced using CAD (Computer Aided Design) software and can, therefore, be changed at any time. Subsequently, the model is saved in the STL (Standard Tessellation Language) file format, thus linking the 3D software and the AM device. Using the STL file format, the surface of the body is approximated by triangles: the smaller the size the better the original geometry of the body. During the AM process, the desired product is built up layer-by-layer, based on the 3D CAD model **[1,2]**. The process of forming by the product is shown in **Figure 1.**

During this process, the powder diffuser disperses a layer of dust on the powder coating which is melted by a high-performance laser according to the desired geometry. As soon as a layer is completed, the pattern is lowered, the powder diffuser creates a new layer that the laser scans again, and this process repeats until the product is ready.

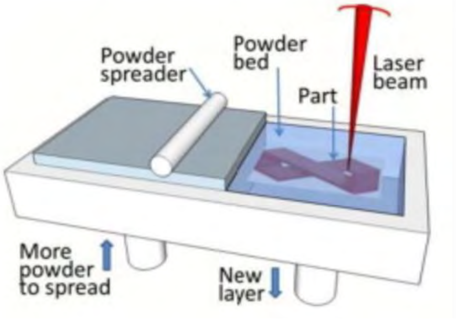

Figure 1. *Process of forming the product [3]*

In our research, the specimen was formed by direct metal laser sintering (DMLS). This procedure is used in several areas, including the field of medicine. In this sector, a basic requirement is that the base material is bio-compatible with the human organism in order to avoid complications after the implant is integrated.

In related research, replacement of a missing part of a skull was completed with DMLS technology. One of the great advantages of AM is the making of custom products. Custom implants can be created by a porous structure that conforms to the geometry of the skull, as shown in **Figure 2.**

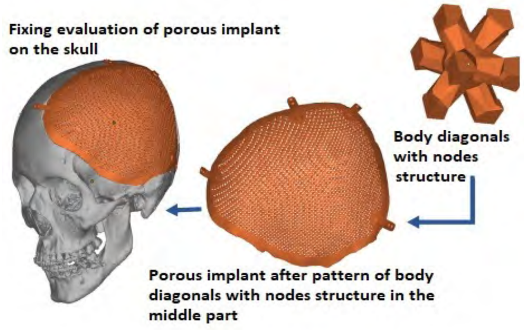

Figure 2. *The shape of the skull implant [4]*

2. Test materials, procedures

The main purpose of our research is to compare the corrosion resistance of two difference test specimens. The first specimen is a Eucatech CCFlex type 4.00x28 mm Co-Cr alloy coronary stent whose base material was produced by conventional powder metallurgy. The second specimen is an EOSINT M280 titanium (Ti-6Al-4V) primary commodity cylindrical body which was made by DMLS. In this case, a Biologic SAS type SP-150 potentiostat was used to measure potential-difference on the two test specimens. The first test used cyclic voltammetry on the stent. Subsequently, the Tafel plot was calculated both on the stent and the titanium specimen. During the measurements 0.9% NaCl physiological saline was used. Before and after the corrosion tests, weight measurement was performed with an APX-200 precision balance and pictures were taken with an Olympus SZX16 stereo-microscope and Zeiss EVO MA10 scanning electron microscope (SEM).

3. Evaluation of results

Table 1. shows the weight loss due to corrosion, which proves the penetration of metal into the solution.

The stereo-microscopic image in **Figure 3.** shows the surface of the stent before and after the corrosion test. After the measurement, general corrosion was observed on the entire surface of the stent.

Figure 4. shows scanning electron microscopy (SEM) pictures of the stent after the corrosion test.

Table 1. *Weight before and after the corrosion test*

	Before corrosion test	After corrosion test
Co-Cr (L605)	0.0246 g	0.0231 g
Ti-6Al-4V	0.1540 g	0.1539 g

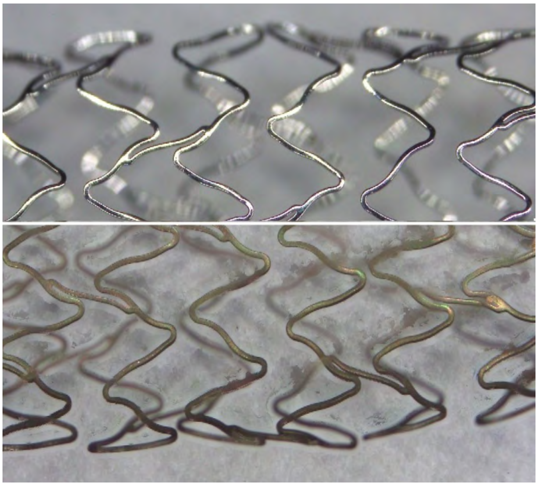

Figure 3. *Surface of the stent before corrosion (above) and after corrosion (below)*

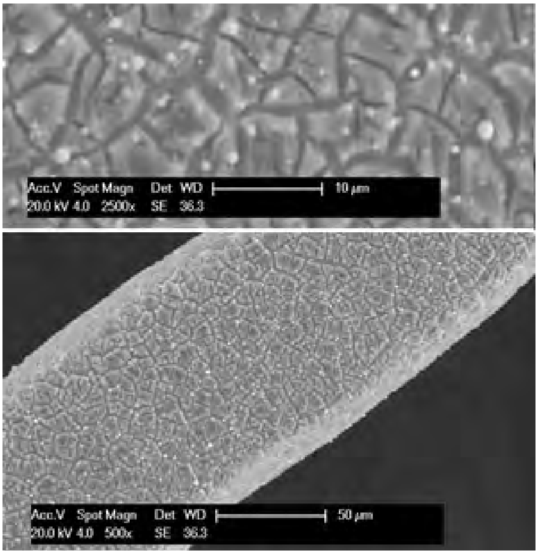

Figure 4. *Scanning electron microscopy images of the stent after the corrosion test*

The stent's base material is made by powder metallurgy, so the tiny white point-like appearances are tungsten-rich segregations, as can be seen in **Figure 4.**

Figure 5. shows the hysteresis curve of cyclic voltammetry and a cathodic and anodic peak potential: E_k = –7.25 mA, E_a = –12.95 mA was determined. In doing so, the passive layer on the stent passes into the solution and a steady state is formed.

Thereafter, the Tafel curve of the stent was determined, as shown in **Figure 6.** After software evaluation with the stent composition, we determined the corrosion rate: $5.72 \cdot 10^{-3}$ mm/year.

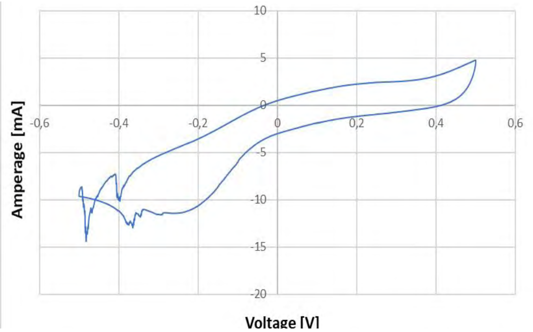

Figure 5. *Cyclic voltammogram of the stent*

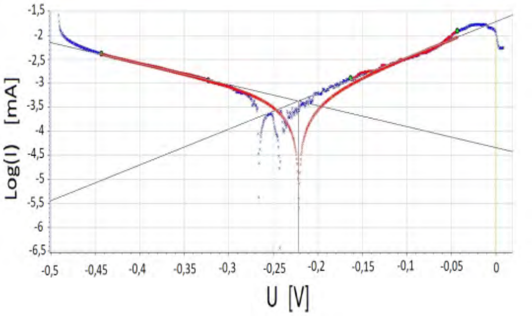

Figure 6. *Tafel plot of the stent*

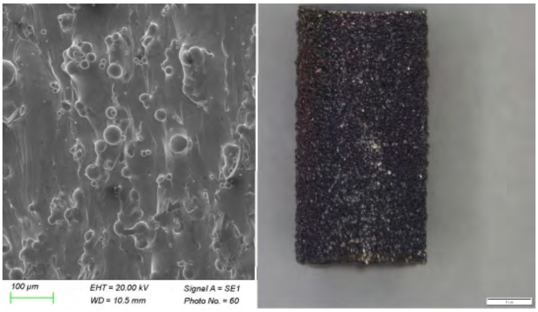

Figure 7. *Titanium cylinder surface SEM (left) and stereomicroscopy (right)*

In **Figure 7.** the SEM and stereomicroscopic image of the additive sample also shows an uneven surface formed by DMLS technology. This uneven surface originated from the melting of the powder material and then random solidification. This microtopography greatly increases the outer surface of the specimen, so the precise surface area is difficult to determine and corrosion processes are affected.

Figure 8. shows that the Tafel curve of the titanium sample differs greatly from the stent Tafel curve. The corrosion rate, in this case, was $2.27 \cdot 10^{-3}$ mm/year.

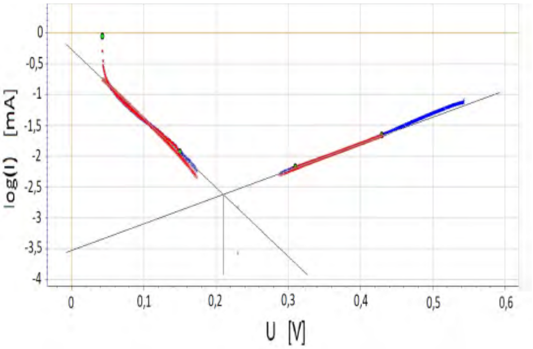

Figure 8. . *Tafel plot of Ti-6Al-4V sample*

4. Conclusions

From the measurement results we can conclude that in the case of NaCl 0.9 % solution, the stent was less resilient with the same corrosion test parameters than the Ti-6Al-4V sample. This is evidenced by the fact that, after corrosion, a relatively large mass decrease was observed in the case of the stent, while in the Ti-6Al-4V sample it was not, and the corrosion rate from the Tafel curve was 2.5 times higher on the stent.

Our test method is appropriate for evaluating additional samples. Among our plans, we compare our results with additive manufactured Co-Cr alloy samples and bulk Ti samples.

Acknowledgements

The project is funded by the National Research, Development and Innovation (NKFIH) Fund. Project title "Developing a new generation of customized medical implants and medical aids for additive technologies". Application ID number: NVKP-16-1-2016-0022. The developers are grateful for the support.

References

[1] Czvikovszky T., Nagy P., Gaál J.: A *polimertechnika alapjai*. Műegyetemi Kiadó, Budapest, 2007.

[2] Gebhardt A.: *Understanding Additive Manufacturing*. Carl Hanser Verlag GmbH & Co. KG, München, 2011.
https://doi.org/10.3139/9783446431621

[3] DebRoy T., Wei H. L., Zuback J. S. et al.: *Additive manufacturing of metallic components – Process, structure and properties*. Progress in Materials Science, 92. (2017) 112–224.
https://doi.org/10.1016/j.pmatsci.2017.10.001

[4] Moiduddin K., Darwish S. et al.: *Structural and mechanical characterization of custom design cranial implant created using additive manufacturing*. Electronic Journal of Biotechnology (2017) 22–31.
https://doi.org/10.1016/j.ejbt.2017.06.005

Acta Materialia Transylvanica 1/2. (2018) 85–88.
https://doi.org/10.2478/amt-2018-0030
Hungarian: ~~https://doi.org/10.2478/amt-2018-0029~~
https://doi.org/10.33923/amt-2018-0029
Corrected: 29.08.2023.

Investigation of Laser Welding Technology of Diamond Drilling Segments

Attila Zsolt KENÉZ,[1, 2] Gyula BAGYINSZKI [3]

[1] *Hilti Tools Ltd., Kecskemét, Hungary, attila.kenez@hilti.com*

[2] *Óbuda University, Doctoral School on Materials Sciences and Technologies, Budapest, Hungary, kenez.attila@phd.uni-obuda.hu*

[3] *Óbuda EUniversity, Donát Bánki Faculty of Mechanical and Safety Engineering, Budapest, Hungary, bagyinszki.gyula@bgk.uni-obuda.hu*

Abstract

Segments containing diamond particles are fixed to replaceable inserts or to steel tool bodies for cost-effectiveness. The joining technology used should meet both environmental and technical requirements. The joining zone is subjected to high mechanical and significant thermal loads during use. In the event of an improper joint, the segments may detach from the base and fly away causing injury. Nowadays, many methods of welding or brazing are used to fix diamond segments. Among the possible segment fixing technologies, laser beam welding has been investigated. The microstructure of the joints has been examined by optical and scanning electron microscopy and chemical element maps have been recorded. Joints have been subjected to fracture and hardness testing. The mechanical properties and composition changes of the joints with different joining technologies have been evaluated and compared.

Keywords: *joining technologies, welding, diamond segment, material testing*

---

1. Introduction

There has been an increased demand from the construction industry for the planned or improvised on-site machining of concrete, requiring tools with a typical application in the areas of chiselling, drilling, wall opening, channelling or surface roughening. These are performed effectively with diamond-edged tools.

At Hilti Tools Ltd. core drill bits with diamond segments [1] are manufactured for a wide range of applications, raw materials and with different performance requirements. The segments are laser welded on the thin walled tube of the core drill bit. In the case of the core bits (diameter range: Ø8…37 mm), a CO_2 laser source is used, while in the case of drill bits (diameter range: Ø40…202 mm) a disk laser source is used for welding.

2. Laser welding

In the small diameter focus spot a very high power density can be achieved, and by absorption, the electromagnetic radiation is transformed into heat in the materials being welded. In a narrow band the heat melts the boundary of the joined pieces and behind the passing radiation a narrow heat-effect, little distortion seam is formed. [2]

Gas laser welding is usually performed with 10,6 μm wavelength (far-infrared) radiation CO_2+N_2+He gas mixture. In this case, CO_2 gas gives rise to the laser's name. [3]

Disc laser welding, e.g. 1,03 μm wavelength (close infrared) radiation, can be achieved by Yb: YAG or Nd:YAG lasers. The Yttrium-aluminium-garnet crystal (YAG) refers to the solid state laser. These lasers have better efficiency compared to CO_2 lasers. [4] [5]

3. Inspections, results

The welded core bits and drill bits have to fulfil their technical requirements. First, we performed non-destructive and destructive tests used in serial production, then the welded bond and the heat affected zone were investigated in more detail.

3.1. Test methods

The non-destructive tests in serial production were as follows:

- Optical inspection: visual inspection of the seam;
- Segment offset (device: dial gauge): the segments have to be positioned on a diameter larger than the outer diameter of the tube;
- segment tilt (device: dial gauge): the parallelism of the segments on the lateral surface of the tube;
- segment twist (device: dial gauge): the difference between the radius of the segment and the radius of the tube;
- radial run out (device: dial gauge): radial run out measured on the surface of the segment while rotating the core drill bit.

Destructive tests used in serial production:

- breakage test (device: digital torque wrench) an insert (in a fitting shape), which is connected to the torque wrench is put on the segment of the product to be examined. After resetting the wrench the segment is broken off and the displayed value read, which has been converted into the position of the breakage.

The welded bond and its environment are examined by the following methods:

- optical light microscope inspection;
- Scanning Electron Microscope, SEM inspection;
- Energy Dispersive Spectroscopy (EDS);
- Hardness measurement with Vickers method.

3.2. Inspection results

Based on the optical microscope investigation the following can be concluded:

- the geometry of the examined samples' welding seam (**Figure 1.** and **2.**) is similar;
- gas inclusions (**Figure 3.**) occur in the welding seams.

After the performed SEM investigation the following can be concluded:

- in some cases crack-like patterns can be observed (**Figure 4.**);
- in the case of C, Mn, Si no significant difference can be seen between the specific zones (**Figure 5.**);
- although from the neutral zones nickel is alloyed into the seam (**Figure 6.**).

In the course of the line analysis, we scanned the specimen along a line with the electron beam (**Figure 7.**).

Figure 1. *Stereo microscope recording of the laser welded seam from the crown side*

Figure 2. *Stereo microscope recording of the laser welded seam from the root side*

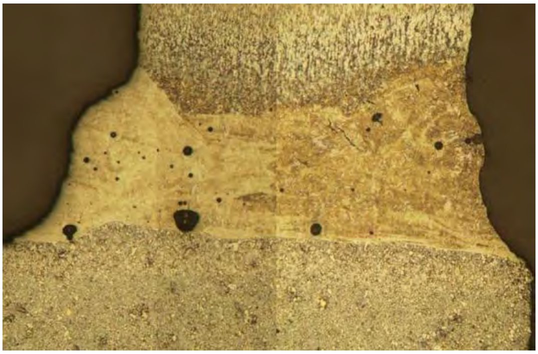

Figure 3. *Optical microscope recording of the laser welded seam*

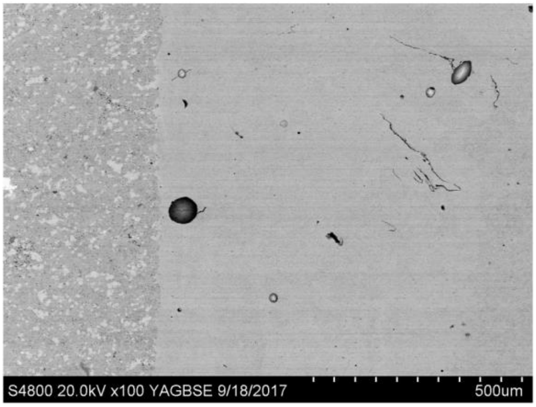

Figure 4. *SEM recording from the middle zone of the laser welded bond*

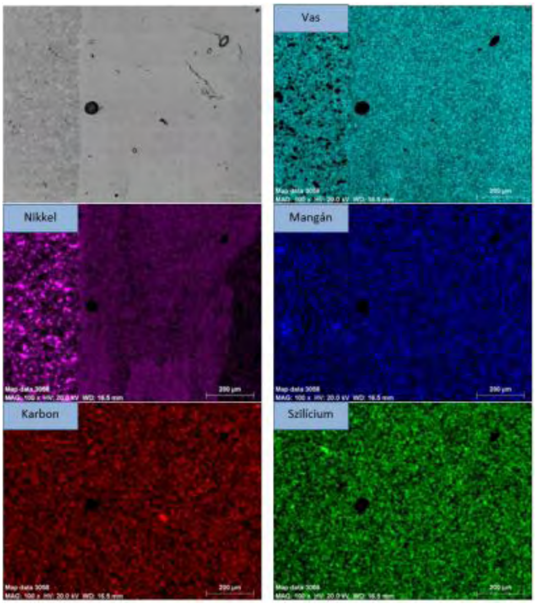

Figure 5. *Element map from the middle zone of the laser welded bond*

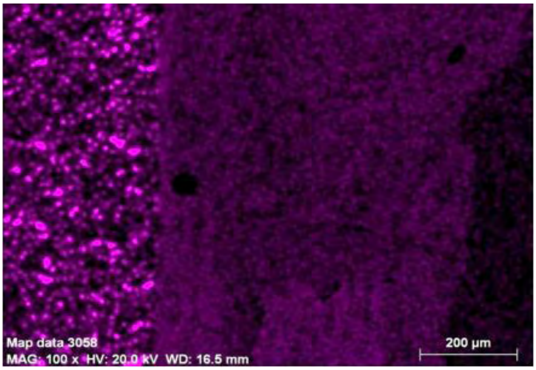

Figure 6. *Ni element map from the middle zone of the laser welded bond*

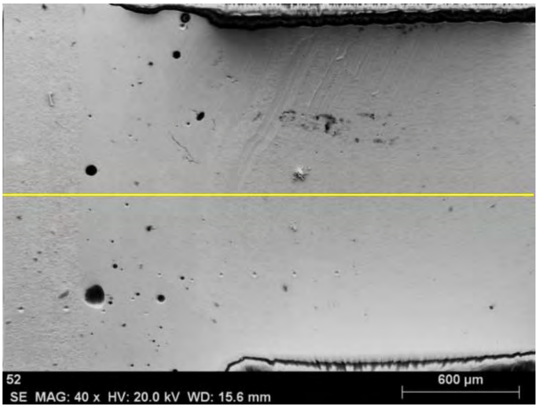

Figure 7. *SEM recording of laser welded bond, the thin yellow line indicates the place of the line analysis (close to the root)*

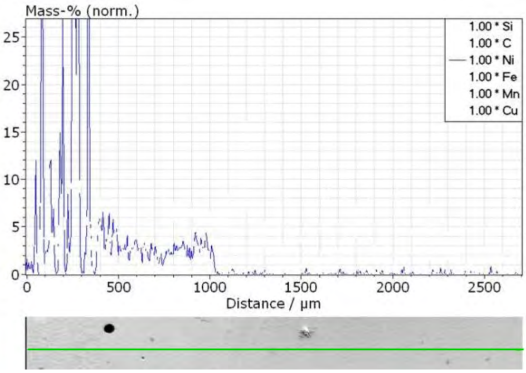

Figure 8. *Laser welded bond's nickel concentration perpendicular to the seam's line in the middle of the seam*

The Energy Dispersive Spectroscopy (EDX) gathers the different energy level X-ray photons (this will be the EDX spectrum) and along the line, for every point, the measured EDX spectrum is assigned.

The concentration of the nickel atom is proportional to the energy level count of the nickel atoms on the EDX spectrum. Changing the electron beam can cause changes in the energy level count, so in the case of two or more fields of view the counts cannot be compared.

Due to this, we determined the specimen's raw material and alloying elements with a full territorial analysis. During the line analysis each element count has been recorded and after normalization, to 100% we derived the nickel (and all the other elements') true percentage by mass.

In **Figure 8.** only the distribution of nickel can be seen. The start of the line analysis always starts from the powder metallurgy raw material, where nickel particles can be seen as well, thus, at the beginning of the analysis peaks can be seen reaching almost 100% (the top of the peaks cannot be seen), but the vertical scale's maximum has been set to 25% so the low concentration nickel in the seam can be also read from the diagram.

4. Consequences

The presented recordings and the inspection results demonstrate the chosen and applied methods of the research.

It can conclude, the applied experimental methods are able to inspect the laser welded and by other type joints, and it can extend by other material tests (like hardness tests).

References

[1] Vincent C.: *Apparatus and Method for Securing Diamond Segment to Rotating Tool.* US 2005/0279533 A1, 2005.

[2] Bagyinszki Gy., Bitay E.: *Hegesztéstechnika I. Eljárások és gépesítés*. EME, Cluj-Napoca, 2010. https://eda.eme.ro/handle/10598/15437

[3] Kovács T.: *Laser welding process specification base on welding theories*. Procedia Manufacturing, 22. (2018) 147–153.

[4] Bitay E.: *Lézeres felületkezelés és modellezés*. EME, Cluj-Napoca, 2007. https://eda.eme.ro/handle/10598/8923

[5] Bagyinszki Gy., Bitay E.: *Nagy energiasűrűségű eljárások hegeszthetőségi szempontjai*. In: Fiatal műszakiak tudományos ülésszaka XVII., Cluj-Napoca, Romania, Műszaki Tudományos Füzetek, 2012. 13–18. https://eda.eme.ro/handle/10598/15489

Acta Materialia Transylvanica 1/2. (2018) 89–92.
https://doi.org/10.2478/amt-2018-0032
Hungarian: ~~https://doi.org/10.2478/amt-2018-0031~~
https://doi.org/10.33923/amt-2018-0031
Corrected: 29.08.2023.

Addictive and Substractive Combined Production of Cobalt-Crome-Based Frames in Dentistry

Kónya János,[1] Kulcsár Klaudia[2]

Dent-Art-Technik Kft., Győr, Hungary
[1] *janos@dentarttechnik.hu*
[2] *kulcsar.klaudia@dentarttechnik.hu*

Abstract

The following study analyses the use of modern 3D printing technology in dentistry with its necessary manufacturing and machining processes. Fitting of the manufactured metal structures is examined depending on their use, in terms of conventional adhesion-based denture designs and screw-fixed dentures on implants. Influencing factors and effects of the required post-processing steps are examined. Aspects such as sand-blasting, heat treatment, equipment and tools required for cutting are analyzed. The aim of this study is to create a manufacturing process that enables the required precision fitting of the created frame structure types.

Keywords: *additive manufacturing, 3D printing, CNC milling, print and mill, CoCr frame structure.*

---

1. Introduction

The possibility of the technological use of 3D printing and the penetration of this technology in dental practice make it indispensable to study the increasingly precise and accurate fitting of metal frame structures in a necessary and sufficient way [1, 2]. Cases presented in this study were analyzed after the execution of concrete work projects. Fitting evaluation tests were carried out using in vitro models in our dental technician laboratory. Oral in vivo tests were carried out in a medical environment. The aim of this study was to analyze the surface characteristics of additively manufactured metal structures. A great emphasis was put on the factors affecting nesting precision, such as support structures, surface roughness in different directions and positions, and other deviations [3, 4, 13]. Thus, the compensation of the virtual design before printing, the potential printing adjustment, and the necessity of subtractive processes arising from the function and fixation of the frame structure could be determined [5, 6].

2. The process of 3D printing

2.1. Material

During additive manufacturing, the dental Co-Cr alloy is used as the material of structural frames for dental prostheses [3, 7, 8].

Manufacturer: BEGO, type: Mediloy S-Co, 5, ISO 22674 and ISO 9693-1. Chemical composition: Co63.9 Cr24.7 W5.4 Mo5.0 Si1.0 (%) grain size: 10–45 µm.

2.2. Sisma MySint 100 and the process of metal-powder printing

A Sisma MySint100 printing unit, using LMF (Laser Metal Fusion) technology, was used for our experiments. During printing, additive and systematic layer-by-layer fusion of 20 µm-thick metal powder particles takes place (**Figure 1.**). Fusion is achieved by using a scanning laser with a focal point of 55 µm, and a power of 90 W. Design of printable products is performed with the help of free surface modelling programs. Post-processing takes place manually, with hand-operated polishing equipment.

Figure 1. *The 3D printing workspace*

3. Fitting requirements of 3D-printed frame structures

We distinguish between the creations of two significantly different products. The first one represents conventional metal-structure dental prostheses fixed to the refined abutments with adhesive bonding. The other represents fixed, metal-structure prostheses where implants are used as fixation pillars for the prosthesis, and structural integrity is warranted by detachable screw-joints. In the case of the same printing parameters in both products, we can expect the same printing defects. These can be an average geometric defect, surface roughness defect, imprecision due to the support material, and technological defect. Based on manufacturer's data and own measurement experiences, its total extent is under 35 μm [1, 4].

3.1. Factors affecting the nesting of adhesion-bonded frame structures

The typical anatomical property of pillar teeth is resilience, which is the elastic nesting in the periodontium allowing 30-50 μm shifting [10]. Another influencing factor is the fixation on pillar teeth, which is generally done with glass ionomer cement with an average grain size of 35-40 μm [1]. For this, an 80-100-μm-wide adhesion gap is created during the design procedure. The typical extent of imprecision is under 35 μm for the 3D-printed frame structure. Because of this, manufacturing imprecision can be eliminated with minimal resilience together with the use of adhesive material [4]. There is no need to calculate using the minimal factors resulting from the elasticity of the frame structure [5].

3.2. Factors affecting the nesting of screw-fixed implant-pillar frame structures

The anatomical resilience of implant pillars that is not followed by compression necrosis of surrounding bone tissue is only 7–8 μm [11]. The second affecting factor is the nesting of the fitting surface of 2-piece implants. It can be fixed on a platform or a taper and requires precise, positioned fitting with an average value of less than 5 μm. Improperly closed implant nesting surfaces can be susceptible to the formation of adverse bacterial flora. It can result in peri-implantitis in the neighbouring tissue and loss of the implant. In this case, elastic deformation, which has an average value of 10–15 μm on peripheries of the complex multi-pillar-supported frame structure also plays an important role [9]. Its evaluation is carried out with Sheffield tests. Refining post-milling of 3D-printed parts is required based on the obtained data [2, 12].

4. The combined use of additive and subtractive technologies

The condition of their use is the expanding or offsetting the pre-defined milling surface with a surface allowance. This offsetting procedure is carried out during design in a parametric support program. The designed allowance provides excess material for post-milling process and deviation compensation. In the next step, during the printing platform design, auxiliary units are added to the frame structure model. They are needed for "zero-point" positioning in the milling machine. This modi-fied printing composition is then uploaded to the 3D printing machine. After the printing process, parts are sand-blasted to correct sur-face roughness. Afterwards, heat treatment is carried out with modified parameters. These parameters were determined using data from experiments evaluating the strength and structure of materials. Based on data of former material tests, it was proven that the me-chanical properties of 3D-printed metal struc-tures, heat treated according to the recom-mendations of the manufacturer, can be im-proved to achieve better metal cutting circum-stances. The aim of the heat treatment is to achieve such a modified material structure during stress relieving that is more easily ma-chinable during precision post-processing (**Figure 2.**).

Four modified heat treatment strategies were defined. [7]. After printing and heat treating of the specimens, tensile and hardness tests were performed (**Table 1.**). Experimental and metallographic data, comparable to our CoCr alloy, were used. **Table 2.** shows the chosen technological parameters of heat treatments measured in a real-life environment in a Nabertherm P330 heat treat furnace.

Figure 2. *The Nabertherm P330 heat treatment oven during use*

Table 1. *Mechanical properties of the result*

	Yield strength (MPa)	Fracture strain (%)	Elastic modulus (MPa)
Manufacturer	923	7.40	39 180
Modified	1003	16.06	33 804

Table 2. *Heat treatment modification*

Heat treatment		Modified heat treatment	
Start temperature	650 °C	Start temperature	650 °C
Heating: 18 min	800 °C	Heating: 38 min	900 °C
Heating: 15min	800 °C	Heating: 28min	900 °C
Cooling: 60 min	550 °C	Cooling: 75 min	550 °C

5. Precision post-processing

5.1. Manufacturing unit

The Vhf S1 simultaneous 5-axis dental milling machine operates a water-cooling system. Thus, it is capable of machining both CoCr and titanium materials. It is characterized by a 0.6 kW spindle, small dimensions, and a high repeat accuracy of ±0,003 mm.

5.2. Tools

The outstanding quality of OSG Dental Industry diamond coating provides an extended application area for tools in dental metal processing [1, 5]. Because of the modified heat treatment parameters, our OSG Dental Industry tools are more durable, and capable of performing the machining protocol in a more tool-saving way (**Figure 3.** and **4.**)

Figure 3. *Geometry and surface before postproduction*

Figure 4. *The implanted fitting surface after processing*

Figure 5. *Frame structures of dental restorations with finished contact surfaces*

6. Summary

Using the results of heat treatment and the possibility of 3D-printed frame structure post-milling, implant-fixed dental prostheses, which are used in dental technician practice, can be created with the fitting precision as determined in our study (**Figure 5.**).

References

[1] Nelson N., K. S. J., Sunny K.: *Marginal Accuracy and Internal Fit of Dental Copings Fabricated by Modern Additive and Subtractive Digital Technologies*. The European Journal of Prosthodontics and Restorative Dentistry, 25/1. (2017) 20–25. https://doi.org/10.1922/EJPRD_01611Nelson06

[2] Joda T., Ferrari M., Gallucci G. O., Wittneben J. G., Brägger U.: *Digital technology in fixed implant prosthodontics*. Periodontol 2000, 73/1. (2017) 178–192. https://doi.org/10.1111/prd.12164

[3] Kim K. B., Kim J. H., Kim W. C., Kim J. H.: *Three-dimensional evaluation of gaps associated with fixed dental prostheses fabricated with new technologies*. The Journal of Prosthetic Dentistry, 112/6. (2014) 1432–1436. https://doi.org/10.1016/j.prosdent.2014.07.002

[4] van Noort R.: *The future of dental devices is digital*. Dental Materials, 28/1. (2012) 3–12. https://doi.org/10.1016/j.dental.2011.10.014

[5] Kim D. Y., Kim J. H., Kim H. Y., Kim W. C.: *Comparison and evaluation of marginal and internal gaps in cobalt-chromium alloy copings fabricated using subtractive and additive manufacturing*. Journal of Prosthodontic Research, 62/1. (2018) 56–64. https://doi.org/10.1016/j.jpor.2017.05.008

[6] Yan X., Lin H.: *Research progress in CoCr metal-ceramic alloy fabricated by selective laser melting*. Zhonghua Kou Qiang Yi Xue Za Zhi, 53/2. (2018) 141–144. https://doi.org/10.3760/cma.j.issn.1002-0098.2018.02.017

[7] Barazanchi A., Li K. C., Al-Amleh B., Lyons K., Waddell J. N.: *Additive Technology: Update on Current Materials and Applications in Dentistry*. Journal of Prosthodontics, 26/2. (2017) 156–163. https://doi.org/10.1111/jopr.12510

[8] Kassapidou M., Franke Stenport V., Hjalmarsson L., Johansson C. B.: *Cobalt-chromium alloys in fixed prosthodontics in Sweden*. Acta Biomaterialia Odontologica Scandinavica, 3/1. (2017) 53–62. https://doi.org/10.1080/23337931.2017.1360776

[9] de França D. G., Morais M. H., das Neves F. D., Carreiro A. F., Barbosa G. A.: *Precision Fit of Screw-Retained Implant-Supported Fixed Dental Prostheses Fabricated by CAD/CAM, Copy-Milling, and Conventional Methods*. The International Journal of Oral & Maxillofac Implants, 32/3. (2017) 507–513. https://doi.org/10.11607/jomi.5023

[10] Fehér E., Gallatz K., Gerber G., Székely A. D.: *Maxillofacialis anatómia*. Medicina Könyvkiadó Zrt., Budapest, 2014. 79–9.

[11] Ihde S. K. A., Ihde A. A.: *Bevezetés a Stratégiai Implantátumok használatába*. International Implant Foundation Publishing, München, 2016.

[12] Marková K., Mitrushchenkov Y., Idhe S. K. A., Idhe A. A.: *Stratégiai implantátumokon végzett technikai munkafázisok*. International Implant Foundation Publishing, München, 2016.

[13] Redwood B., Schöffer F., Garret B., *The 3D Printing Handbook*. 3D Hubs B.V., Amsterdam, 2017. 123–133, 213–215.

Acta Materialia Transylvanica 1/2. (2018) 93–96.
https://doi.org/10.2478/amt-2018-0034
Hungarian: ~~https://doi.org/10.2478/amt-2018-0033~~
https://doi.org/10.33923/amt-2018-0033
Corrected: 29.08.2023.

Application of High Energy Absorbing Materials for Blast Protection

Tünde KOVÁCS,[1] Zoltán NYIKES,[2] Lucia FIGULI[3]

[1] *Óbuda University, Donát Bánki Faculty of Mechanical and Safety Engineering, Institute of Materials and Manufacturing Sciences, Department of Materials Technology, Budapest, Hungary, kovacs.tunde@bgk.uni-obuda.hu*

[2] *Óbuda University, Doctoral School on Safety and Security Sciences, Budapest, Hungary, nyikes.zoltan@phd.uni-obuda.hu*

[3] *University of Zilina, Faculty of Security Engineering, Department of Technical Science and Informatics, Zilina, Slovakia, lucia.figuli@fbi.uniza.sk*

Abstract

In the current century, building protection is very important in the face of terrorist attacks. The old buildings in Europe are not sufficiently resilient to the loads produced by blasts. We still do not fully understand the effects of different explosives on buildings and human bodies. [1–3] Computing blast loads are different from that of traditional loads and the material selection rules for this type of impact load are diverse. Historical and old buildings cannot be protected simply by new walls and fences. New ways need to be found to improve a building's resistance to the effects of a blast. It requires sufficiently thin yet strong retrofitted materials in order to reinforce a building's walls [4–6].

Keywords: *metal foam, energy absorbing, building protection, reinforced composite.*

---

1. Introduction

In Europe, many terrorist attacks have caused notable damage. The NATO and V4 countries are currently working to secure the safety of citizens, critical infrastructure and buildings [6–8]. The challenge of our age is to innovate and invent new materials for these special loads: loads that didn't have to be considered previously. Extraordinary loads, such as those produced by blasts, are combined load because they involve various parameters, including shock waves and scatters. Blast effects from a detonation produce building damage and fragmentation effects. The initial explosion produces secondary damage, caused by fragments of brick and other materials striking other buildings and human bodies [1–3].

Compared to static loads, the blast effect of such high-speed plastic deformation can produce different behaviour in the materials.

The properties of traditional materials under static loads are well understood and tested. This knowledge forms the basis of the design of these constructions.

However, the material selection and design for dynamic and extreme loads are not yet well defined, from the testing method point of view, or the material properties point of view.

2. TNT equivalent determination

The wave and heat energy caused by a blast depending on the blast range and chemical composition. Determining the TNT equivalent is useful for designing the load *(1)* [3, 8]:

$$W_{TNT} = \left(\frac{\Delta H_{EXP}}{\Delta H_{TNT}}\right) W_{EXP}(kg) \qquad (1)$$

where:

W_{TNT} (kg)) is the TNT volume equivalent mass,
ΔH_{EXP} (MJ/kg) is the blasting heat,
ΔH_{TNT} (MJ/kg) s the TNT blast heat,
W_{EXP} (kg) is the calculated explosive mass.

Table 1. shows the performance of some explosives.

Table 1. *Performance of some common explosives [8, 9]*

Name of the explosive	The energy of the blast (MJ/kg)
TNT	4.1–4.55
C4	5.86
RDX	5.13–6.19
PETN	6.69
Pentolite 50/50	5.86
Nitro-glycerine	6.30
Nitrocellulose	10.60
Amon/Nitrate	1.59

3. Determination of the blast pressure

We already know some equations for determining the blast load. The most useful for load design is the Hopkinson-Cranz law *(2)* [8, 9].

$$Z = \frac{R}{\sqrt[3]{W}} \quad \left(m \cdot kg^{-\left(\frac{1}{3}\right)} \right) \tag{2}$$

where the distance of the blast determination of the object is Z (mkg$^{-(1/3)}$) from the W (kg) explosive mass volume for TNT equivalent.

The Mills equation for nascent gas pressure determination *(3)*, where W is the explosive mass in the TNT equivalent (kg), R is the explosive distance from the object (m):

$$P_{SO} = \frac{R}{Z^3} - \frac{R}{Z^2} + \frac{R}{Z} \quad (kPa) \tag{3}$$

The blast establishes a short pressure load followed by a longer duration of a vacuum effect. The design load is calculated from the pressure. The blast load parameters can be obtained from the literature **[8].** fThe maximal pressure shows the pressure and vacuum loads in the case of the blast, shown in **Figure 1.** láthatóak. A nyomó és húzó igénybevételek egy robbanás esetén kerülnek bemutatásra.

4. Classical Lamination Theory (CLT)

For designing composite materials classical lamination theory knowledge is required. Based on this theory and design rules we can manufacture a new composite for static and dynamic loads but for blast load we cannot identify design rules. In our research, the classical design rules are the basis of the blast resisting materials design. Based on the practical impact test results we are able to develop the design rules for blast resistant composites.

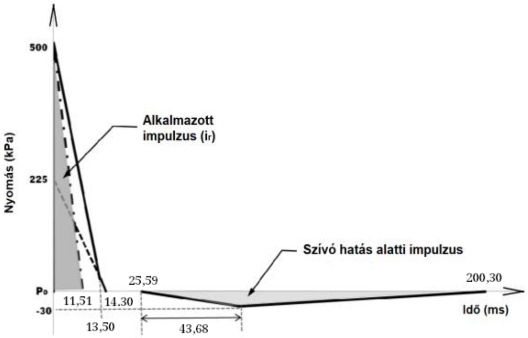

Figure 1. *Front wall pressure and time curve [8]*

Design method steps are as follows [4]:

1. Calculation of the stiff parts of the matrix (Q) for all layers,
2. Determination of the loads,
3. Calculation of the layer plane deformation (ε_{xx}, ε_{yy}, γ_{xy}),
4. Determination of the stress in all layers (σ_{xx}, σ_{yy}, τ_{xy})
5. Calculation of the layer's elastic constant (E_{xx}, E_{yy}, ν_{xy}, ν_{yx}, G_{xy})
6. Determination of the average effective strength base on the damage parameters.

In our case of the next special material, this theory was applied (CLT). The load is combined including high pressure and high energy impact.

5. Testing of specific composite for blast protection

For the protection of buildings, a new retrofit technique is required. The new materials innovated by material science can provide a good solution for this project task. These materials are usually composite, such as syntactic foams, spherical shells or carbon field reinforced composites [4–6]. Some common retrofit techniques have been introduced in previous work which focused on the practical aspects of retrofit techniques used for the blast protection of buildings. It presents the summary of various retrofit techniques [12, 14]. In the case of the introduced extraordinary dynamic loads, we needed to select or innovate a high kinetic energy absorbing material. The metal foams and the composites can be useful for absorbing these loads.

In the following innovation, we introduce a polymer sandwich composite, reinforced by ceramic spherical shells with a glass woven structure.

One of the steps of manufacturing the sandwich structured polymer is shown in **Figure 2.**

Figure 3. shows a prepared sample for testing. The introduced composite has layers of ceramic spherical shells combined with a gas woven structure. Ceramic spherical shells are 0.8 mm (average) diameter, the glass fibre woven structure is 390 g/m2 and the matrix material is epoxy resin (Araldite LY 1564). There were 15 unidirectional and isotropic layers. The dynamic effect was simulated by the Charpy impact test.

The result of the Charpy impact test is shown in **Figure 4.** It is obvious that the tested sample didn't break under the applied load. The test method used can give us information about the dynamic load effect of such materials.

6. Conclusion

Based on the practical impact test results and the experimented test samples we detected that the ceramic spherical shell diameter was important for kinetic energy absorption. We tested three different ceramic spherical shell diameters of reinforced composites (diameters: 0.15 mm, 0.8 mm, 1.5 mm). The kinetic absorption depended on the ceramic spherical shell diameter, the smallest caused a reduced kinetic absorption level. In the case of the larger diameter spherical shells this property improved but in the case of the open spherical shells, stuffed with acrylic, the kinetic absorption level was reduced. This effect caused a moderate improvement in the kinetic energy absorption level. Finally, we can conclude that the middle sized spherical shell diameter improved the kinetic absorption level.

The introduced composite material shows the method to follow for blast resistant material innovation. Furthermore, the implemented composite design rules can be a basis of new material designs.

Moreover, the recycling possibility of these materials is an important aspect, as is shown in **[13]**. In the case of the introduced material, this prerequisite wasn't attainable.

Based on these practical and theoretical results, we are planning to continue with the innovation in new blast-resistant composite materials.

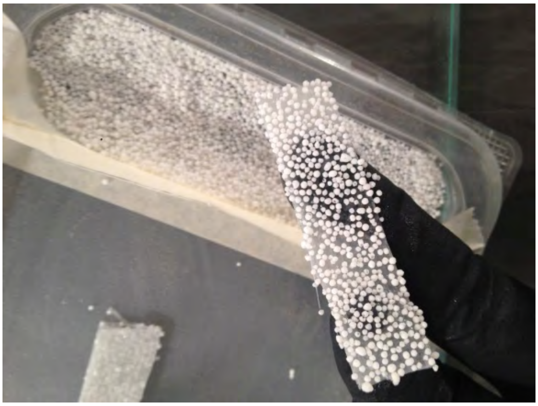

Figure 2. *One of the manufacturing steps of the ceramic spherical shells and glass woven structure reinforced composite [10]*

Figure 3. *Ceramic spherical shells and glass woven structure reinforced composite [10].*

Figure 4. *Picture of the sample after dynamic impact load [11]*

Acknowledgement

The authors would like to thank András Bezzeg and Ákos Végh KANDSI Kft. (AKOBEZ) for the composite manufacturing and also thank Ágoston Balázs for the Charpy test investigation.

References

[1] Lu G., Yu T.: *Energy absorption of structures and materials*. Woodhead Publishing, Cambridge, England, 2003. 317–351.

[2] Uddin N.: *Blast protection of civil infrastructures and vehicles using composites*. Woodhead Publishing Limited, 2010.

[3] Conrath E. J. et al.: *Structural Design for Physical Security State of the Practice*. Structural Engineering Institute, US, Virginia, 1999. Chapter 2. 1–34.

[4] Ashby M.F. et al.: *Metal Foams: A design Guide*. Butterworth-Heinemann, 2000.

[5] Vaidya U. K.: *Impact Response of Laminated and Sandwich Composites*. In: Impact Engineering of Composite Structures. (ed.: Serge Abrate et al.). CISM 526., Springer, Vienna, 2011. 97–191. https://doi.org/10.1007/978-3-7091-0523-8_4

[6] Kovács T.: *Épületvédelem nagy energia elnyelő képességű anyagokkal.* In: A XXII. Fiatal műszakiak tudományos ülésszaka előadásai, Cluj-Napoca, Románia, Műszaki Tudományos Közlemények 7., Erdélyi Múzeum-Egyesület, 2017. 247–250. https://eda.eme.ro/handle/10598/29793

[7] Balázs Á., Nyikes Z., Kovács T.: *Building Protection with Composite Materials Application.* Key Engineering Materials, 755. (2017) 286–291. https://doi.org/10.4028/www.scientific.net/KEM.755.286

[8] Karlos V., Solomos G.: *Calculation of Blast Loads for Application to Structural Components*. Publication Office of the European Union (2013) 1–49. http://publications.jrc.ec.europa.eu/repository/handle/JRC87200

[9] Figuli L., Jangl Š., Papán D.: *Modelling and Testing of Blast Effect On the Structures*. IOP Conf. Series: Earth and Environmental Science 44. (2016). https://doi.org/10.1088/1755-1315/44/5/052051

[10] Bezzeg A., Végh Á.: *Kompozit gyártási jegyzőkönyv*. AKOBEZ, Budapest, 2018.

[11] Balázs Á.: *Épületvédelem kompozit anyagokkal.* MSc diplomaterv, OE-BGK, Budapest, 2018.

[12] Figuli L., Štaffenová D.: *Practical aspect of methods used for blast protection.* Key Engineering Materials, 755. (2017) 139–146. https://doi.org/10.4028/www.scientific.net/KEM.755.139

[13] Figuli L., Magura M., Kavický V., Jangl Š.: *Application of recyclable materials for an increase in building safety against the explosion of an improvised explosive device*. Advanced Materials Research, 1001. (2014) 447–452. https://doi.org/10.4028/www.scientific.net/AMR.1001.447

[14] Štoller J., Dvořák P.: *Field Tests of Cementitious Composites Suitable for Protective Structures and Critical Infrastructure*. Key Engineering Materials, 722. (2016) 3–11. https://doi.org/10.4028/www.scientific.net/KEM.722.3

Acta Materialia Transylvanica 1/2. (2018) 97–100.
https://doi.org/10.2478/amt-2018-0036,
Hungarian: ~~https://doi.org/10.2478/amt-2018-0035~~
https://doi.org/10.33923/amt-2018-0035
Corrected: 29.08.2023.

The Influence of Heat Treatment on the Mechanical Properties of 3D-Printed Cobalt-Chrome Alloy Used in Dental Laboratory Practice

Klaudia KULCSÁR,[1] János KÓNYA[2]

Dent-Art-Technik Kft., Győr, Hungary

[1] *kulcsar.klaudia@dentarttechnik.hu*

[2] *janos@dentarttechnik.hu*

Abstract

The material used for manufacturing of dental implantation prostheses is cobalt-chromium alloy. The following study presents a new heat treatment technology for dental implantation prostheses. Specimens were created with the innovative technology of 3D printing. The brittleness of specimens subjected to heat treatment with parameters recommended by the manufacturer made it necessary for us to reconsider the heat-treating process. After changing given heat treatment processes, tensile and hardness tests were performed. From these tests, the optimal heat treatment process technology was chosen.

Keywords: *cobalt-chrome alloy, heat treatment, 3D printing.*

---

1. Introduction

In recent decades, cobalt-chromium alloys have been widely used in casting molds due to their outstanding corrosion resistance, bio-compatibility, and strength [1–3]. Over the years, cobalt-chromium (Co-Cr) alloys have shown remarkable versatility and durability as orthopaedic implant materials [4]. Co-Cr alloys are also used in dental practice e.g. abutments (superstructures), crowns, and bridges [5]. These alloys provide the best balance between mechanical strength and wear resistance. Moreover, their corrosion resistance is also remarkable [6–10]. In the dental field, conventional lost-wax casting techniques have been used for decades. However, these techniques are susceptible to human errors [11]. The production of dental implants is common with conventional methods, for example casting technology [12]. Precision casting and forging still belong to conventional methods in terms of implant manufacturing [13]. On the other hand, additive manufacturing technologies are becoming even more widespread in the production of dental implant prostheses [14]. To make SLM technology suitable for implant or prosthesis manufacturing, certain conditions must be met. The mechanical and chemical properties of the layers created with laser melting of particles must match strict requirements [15]. Mechanical properties and corrosion resistance of alloys processed with SLM (Selective Laser Melting) were studied [16]. Moreover, the strength of the adhesion bond between the ceramic material and Co-Cr alloy was also examined [17].

2. Materials and methods

2.1. Materials used

Type 5, ISO 22674, and ISO 9693-1 dental Co-Cr alloy were used. The chemical composition (% by weight) of cobalt-chromium is shown in **Table 1.**

Table 1. *Chemical composition of Co-Cr alloy*

Element	% by weight
Cobalt (Co)	63.9
Chromium (Cr)	24.7
Tungsten (W)	5.4
Molybdenum (Mo)	5.0
Silicon (Si)	1.0

2.2. 3D printing of specimens

Co63.9Cr24.7W5.4Mo5.0Si1.0 (%) alloy can be the material of choice for implants and pros-theses created with additive manufacturing processes. Test specimens were manufactured with a Sisma Mysint 3D printer. 3D printing is carried out with LMF (Laser Metal Fusion) technology. This technology requires a specific printing strategy. It contains support structures for heat dissipation. A programmable furnace for additional heat treatment was installed nearby the printing unit. Furthermore, a dedicated software and milling machine was available for precision post-processing. Additive manufacturing is preceded by a digital model design. 3D printing is an additive manufacturing technology during which the metal-powder layers are added layer by layer, and the specimens are created with the structured fusion of these layers. The specimen model was designed in a 3D virtual environment and was followed by the printing process that lasted approximately four hours. After printing, specimens are removed from the machine and then separated from the building platform. The heat dissipating support material, which connects the specimens with the disc, is removed afterwards.

2.3. Heat treatment

Following the 3D printing procedure, specimens were subjected to heat treatment with parameters recommended by the manufacturer. **Figure 1.** shows the given heat treatment parameters obtained from the manufacturer. Heat-treating consists of three phases: heating, soaking, and cooling. The proper heat-treating technique is chosen based on the size, geometry, material, and quality requirements of the given part. Hereby, the most important technological parameters can be defined, such as heat-treating temperature and cooling method.

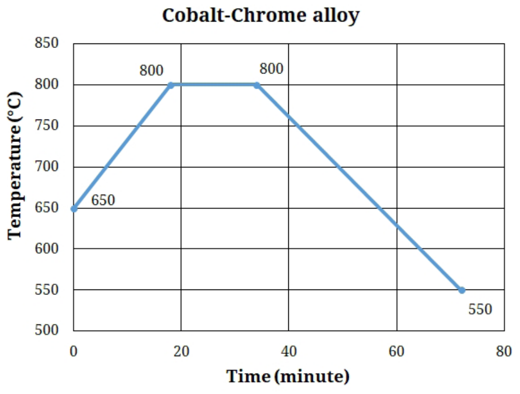

Figure 1. *Heat-treating process provided by the manufacturer*

3. Experiments

Using heat treatment parameters recommended by the manufacturer resulted in a brittle structure, which led to the fracture of some printed specimens. The heat-treating process parameters were changed after this. As a first approach, the heat treating temperature was changed. Numbers in **Table 2** label the following: number 1 indicates the heat treatment process provided by the manufacturer with a maximum temperature of 900°C. Numbers 2 and 4 represent heat-treating processes with a maximum temperature of 900°C. Numbers 3 and 5 mark 1050°C as the maximum temperature. At numbers 3 and 5, process times were changed. Here, all three phases of heat treatment were extended in time.

Changes were determined based on metallographic and experimental data.

Heat treatment marked with number 1 follows manufacturer's recommendations. Based on these experiments, number 4 shows the best solution so far, where fracture strain was increased the most. Thus, elastic modulus decreased, which meant the reduction of the brittleness of the whole structure. **Figure 2.** shows the process diagram for heat treatment labelled with number 4. Number 5 heat treatment had a temperature of 1050°C with a holding time of 118 minutes. No major differences were discovered, but surface oxidation occurred.

AHardness tests were then performed on the specimens. Rockwell hardness was measured in different points of the samples. **Table 3.** shows average hardness values characterizing the specimens.

Table 2. *Mechanical properties obtained after testing*

Number	Tensile strength (Mpa)	Fracture strain (%)	Elastic modulus (Mpa)
1	923	7.4	39 180
2	1041	7.2	47 362
3	1095	7.5	45 302
4	1003	16.06	33 804
5	1097	12.05	34 742

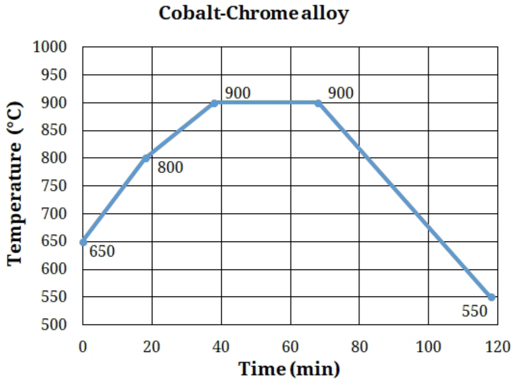

Figure 2. *Heat treatment process*

Table 3. *Mechanical properties measured*

Number	Hardness (HRC)
1	37.37
2	42.3
3	40.04
4	44.88
5	44.4

Table 3. shows the highest average hardness for the specimen marked with number 4. Hardness values measured on specimen number 4 also showed the lowest standard deviation. Other samples showed higher standard deviations during hardness tests. The next step of our research is influenced by the cause of these values.

4. Conclusion

Different heat treatment processes were presented in this study. Our goal was to obtain such mechanical properties for the additively manufactured cobalt-chromium alloy specimens that match dental requirements as precisely as possible. Elastic modulus, which provides information about the stiffness of the material, decreased. The study is going to be continued with the examination of different heat-treating processes. Partial results were achieved.

References

[1] Davis J. R.: *Nickel, cobalt and their alloys*. Materials. Park (OH), ASM International, 2000.

[2] Nasab M. B., Hassan M. R., Sahari B. B.: *Metallic biomaterials of knee and hip: a review.* Trends in Biomaterials and Artificial Organs, 24/2. (2010) 69–82. http://medind.nic.in/taa/t10/i2/taat10i2p69.pdf

[3] Malayoglu U., Neville A.: *Mo and W, as alloying elements in Co-based alloy: their effects on errosion-corroison resistance*. Wear, 259. (2005) 219–229. https://doi.org/10.1016/j.wear.2005.02.038

[4] Monroy K., Delgadio J., Ciurana J.: *Study of the pore formation on CoCrMo alloys by selective laser melting manufacturing process*. Procedia Engineering, 63. (2013) 631–369. https://doi.org/10.1016/j.proeng.2013.08.227

[5] Wataha J. C., Schmalz G.: *Dental alloys*. In: Biocompatibility of Dental Materials. (eds.: Schmalz G., Arenholt-Bindslev D.). Springer, Berlin, Heidelberg, 2009. 221–254. https://doi.org/10.1007/978-3-540-77782-3_8

[6] Kalpana S. Katti: *Biomaterials in total joint replacement*. Colloid Surface B: Biointerfaces, 39/3. (2004) 133–142. https://doi.org/10.1016/j.colsurfb.2003.12.002

[7] Hsu H. C., Lian S. S.: *Wear properties of Co-Cr-Mo-N plasma-melted surgical implant alloys*. Journal of Materials Processing Technology, 138. (2003) 231–235. https://doi.org/10.1016/S0924-0136(03)00077-3

[8] Okazaki Y., Gotoh E.: *Comparison of metal release from various metallic biomaterials in vitro*. Biomaterials, 26/1. (2006) 11–21. https://doi.org/10.1016/j.biomaterials.2004.02.005

[9] Lin H. Y., Bumgardner J. D.: *In vitro biocorroison of Co-Cr-Mo implant alloy by macrophage cells*. Journal of Orthopaedic Research, 22/6. (2004) 1231–1236. https://doi.org/10.1016/j.orthres.2004.04.005

[10] Hsu R. W-W., Yang C.-C., Huang C.-., Chenb Y.-S.: *Electrochemical corrosion studies on Cr-Co-Mo implant alloy in biological solutions*. Materials Chemistry and Physics, 93/2-3. (2005) 531–538. https://doi.org/10.1016/j.matchemphys.2005.04.007

[11] Eggbeer D., Ribb R., Williams R.: *The computer-aided design and rapid prototyping fabrication of removable partial denture frameworks*. Proceedings of the Institution of Mechanical Engineers. Part H: Journal of Engineering in Medicine, 219/3. (2005) 195–202. https://doi.org/10.1243/095441105X9372

[12] Dourandish M., Simchi A., Godlinski D.: *Rapid Manufacturing of Co-Cr-Mo Implants by Three-Dimensional Printing Process for Orthopedic Applications*. Iranian Journal of Pharmaceutical Sciences, 4/1 (2008) 31–36. https://pdfs.semanticscholar.org/9eef/39e3f5ccb9b96171911b399044c201b66f12.pdf

[13] Bertol L. S., Júnior W. K., da Silva F. P., Kopp C. A.: *Medical design: Direct metal laser sintering of Ti-6Al-4V*. Materials & Design, 31/8. (2010) 3983–3988. https://doi.org/10.1016/j.matdes.2010.02.050

[14] Senthilkumaran K., Pandey P. M., Rao P. V. M.: *Influence of building strategies on the accuracy of*

parts in selective laser sintering. Materials & Design, 30/8. (2009) 2946–3294.
https://doi.org/10.1016/j.matdes.2009.01.009

[15] Takaichi A., Nakamotoc T., Jokod N., Numorab N., Tsusumib Y., Migitab S. et al.: *Microstructures and mechanical properties of Co-29Cr-6Mo alloy fabricated by selective laser melting process for dental applications*. Journal of the Mechanical Behavior of Biomedical Materials, 21 (2013) 67–75.
https://doi.org/10.1016/j.jmbbm.2013.01.021

[16] Nan X., Xian-Zhen X., Jie C., Bin W.: *Metal-ceramic bond strength of Co-Cr alloy, fabricated by selective laser melting*. Journal of Dentistry, 40/6. (2012) 453–457.
https://doi.org/10.1016/j.jdent.2012.02.006

[17] Davis J. R. (Ed.): *Cobalt-Base Alloys*. In: Handbook of Materials for Medical Devices. ASM International, Ohio, 2003. 31–37.

Acta Materialia Transylvanica 1/2. (2018) 101–104.
https://doi.org/10.2478/amt-2018-0038,
Hungarian: ~~https://doi.org/10.2478/amt-2018-0037~~
https://doi.org/10.33923/amt-2018-0037
Corrected: 29.08.2023.

The Replacement of Resistance Welding with Laser Beam Welding

Anna MALOVECZKY,[1] Ambrus KARAI[2]

Bay Zoltán Non-profit Ltd. for Applied Research, Budapest, Hungary
[1] *anna.maloveczky@bayzoltan.hu*
[2] *ambrus.karai@bayzoltan.hu*

Abstract

Resistance welding has long been successfully used in the automotive industry, but nowadays, there are even more advanced technologies, such as laser beam welding, which is a much faster, more economical and flexible technology. During our work, we have mapped the possibility of replacing resistance welding with laser beam welding. Furthermore, we have found a solution to the problems occurring during laser beam welding. The biggest challenge in laser beam technology is that the zinc coating on the steel plates (required to prevent corrosion) evaporates during welding, resulting in pores, and leading to a significant reduction in weld strength. We have solved that by using spacer sheets, which allow the zinc vapour to escape from the keyhole.

Keywords: *laser welding, resistance welding, spot welding.*

1. Introduction

Laser beam welding is gaining ground in a wide range of industries [1, 2]. The reason for its spread is in its favourable technological parameters:

- precision, accurate control of the technological parameters;
- high machining speed;
- excellent machining quality (post-processing needs are reduced or cancelled)
- no force affects the work piece;
- wide range of selectable, and precisely con-trollable energy densities in machining;
- small specific thermal stress on the work piece;
- the machining tool is abrasion-free and unaffected by the direction of machining (light);
- excellent automation;
- economical production;
- great manufacturing flexibility;
- good compatibility with other technologies [3].

However, there are a number of challenges in laser beam welding:

Steel sheets are usually coated with a zinc layer for corrosion resistance. Due to the low boiling point of zinc, it vaporizes intensively during welding. Thus, it makes the keyhole unstable and it is able to create such vapour pressure over the weld seam that the molten metal splashes out of the plasma channel (sputtering weld). In addition, zinc vapour bubbles can also be incorporated into the weld. As a result, the weld strength significantly decreases.

During the research, several methods have been tried in order to eliminate the zinc vapour problem [4–23]. However, they have been either ineffective or have made the production too cumbersome. According to our idea, with a plastic forming, small bumps can be created on the surface of the plate, which serves as spacers during the welding process. The experiments were carried out with a spacer sheet solution since the two solutions are the same, but the bumpy version is also in place during manufacturing and industrial applications.

2. Materials and methods

The welding experiments were performed using a Trumpf TruLaser Cell 7020 5D Laser Machining Centre with Trumpf TruDisk 4001 laser radiation source. First, blind welds were made and then steel sheet pairs were welded. Sheet pairs were made using spacer sheets, and also sheet pairs with no gap in between them. The most important welding parameters were the following; laser power 1,000 W, welding speed 3 m / min [24]. The focal point of the laser beam was set to 1 and 4 mm (defocus) relative to the surface of the upper sheet. The plates to be welded were cold rolled, with a thickness of 0.6 mm and with galvanized zinc coating. The thickness of the spacer sheets was 0.1 mm. During welding, the plates were clamped together with the spacer sheets placed between them. For the metallographic examination, the plates were cut with a water-cooled disc cutter, then ground polished and finally etched with 3% nital solution.

A VHX J20 Keyence digital light microscope was used to examine the welds and to take im-ages.

3. Results and discussion

Figures 1-3., show light microscopic images of the welds produced with a 4 mm defocus, and **Figures 4-6.** show images with 1 mm defocus. The most important dimensions of the seams are shown in **Table 1.**

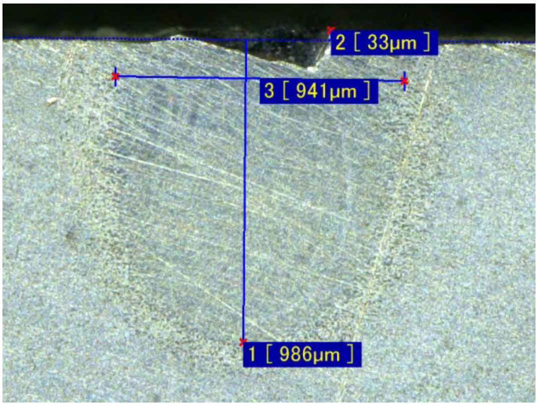

Figure 1. *Picture of blind weld with 4 mm defocus*

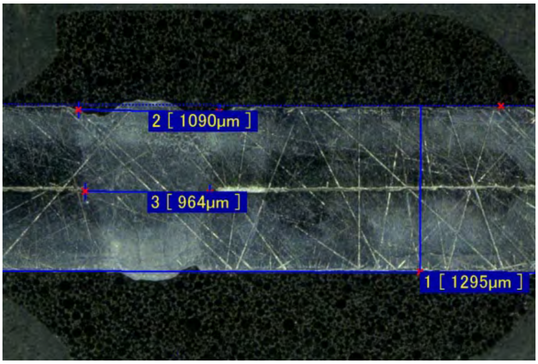

Figure 2. *Picture of weld without gap, with 4 mm defocus*

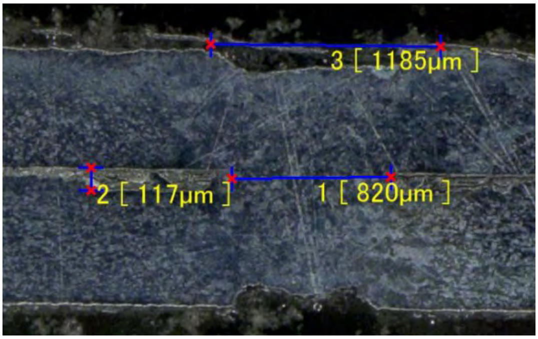

Figure 3. *Picture of weld with spacer sheets, with 4 mm defocus*

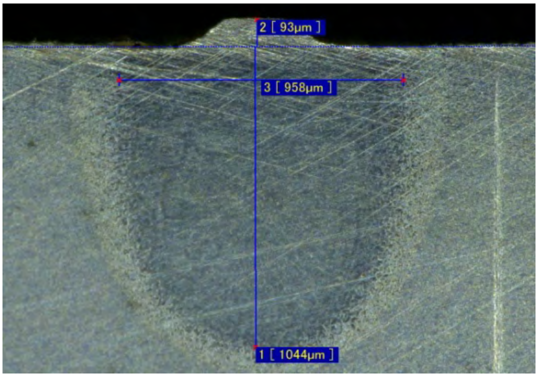

Figure 4. *Picture of blind weld with 1 mm defocus*

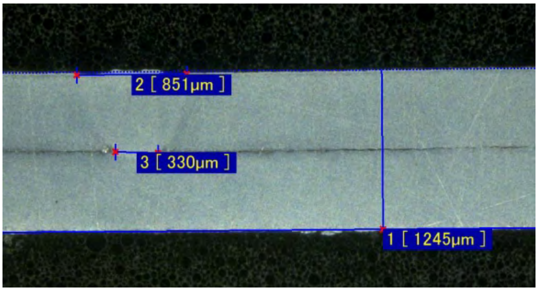

Figure 5. *Picture of weld without gap, with 1 mm defocus*

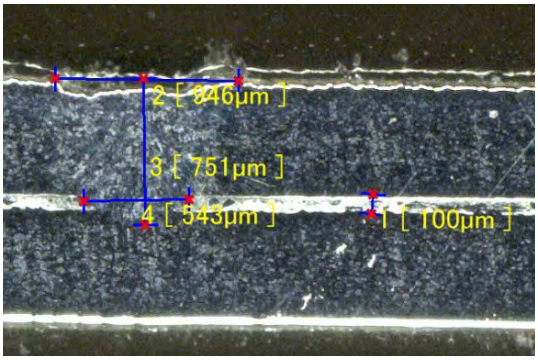

Figure 6. *Picture of weld with spacer sheets, with 1 mm defocus*

Table 1. *Dimensions of the welds*

Defocus (mm)	Type	Weld depth (µm)	Face width (µm)
4	blind weld	986	941
4	without gap	-(melted through)	1090
4	with spacer sheets	-(melted through)	1185
1	blind weld	1044	958
1	without gap	732	851
1	with spacer sheets	751	946

On metallographic images, it is apparent that the 1 mm defocus value yields better results for this type of steel. Indeed, in the other cases (the non-gapped and gapped samples) the bottom plate was melted through because the laser power was too high.

Furthermore, 0.1 mm gaps can be observed in the spacer sheet solution. Splashes and pores are not visible even when the gap is not set because the plates are very thin.

4. Conclusions

The biggest disadvantage of resistance spot welding is that it is not able to adapt quickly to inflexible technology, i.e. fast changes in the automotive industry. Resistance welding is a slow process, and it is costly because heating up the work piece by electrodes requires a large amount of energy input.

Laser welding (especially in the case of re-mote welding) has a high machining speed, is highly automated, combines well with other technologies, and has high manufacturing flexibility. Furthermore, it is very precise, and there is no need for rework. The cost of in-vestment in laser remote welding is higher, but production is much more economical as well as welding parameters can be kept precisely in hand so good weld quality is guaranteed.

Steels are usually coated with a zinc coating for corrosion resistance, but this zinc coating causes serious problems during welding.

During welding, zinc vapour is formed, which incorporates into the weld and makes it porous.

In any case, the high vapour pressure makes the keyhole unstable and it is able to create such vapour pressure over the weld that the molten metal splashes out of the keyhole (sputtering weld). As a result, the weld strength is greatly reduced.

This problem has been solved by installing spacer sheets between the plates so that the zinc vapour could escape. During these test weldings, no splashes or pores were found.

In addition, the appropriate laser parameters have been experimented with for the plate thickness and type of material to be used

Acknowledgements

We would like to thank the Edutus College and its employees who have made it possible for us to carry out our experiments at the premises and to the staff of Bay Zoltán Applied Research Ltd. who supported our work with their advice and help.

References

[1] Bagyinszki Gy., Bitay E.: *Hegesztéstechnika I. Eljárások és gépesítés*. EME, Cluj-Napoca, 2010. https://eda.eme.ro/handle/10598/15437

[2] Bitay E.: *Lézeres felületkezelés és modellezés*. EME, Cluj-Napoca, 2007. https://eda.eme.ro/handle/10598/8923

[3] Búza G.: *Lézersugaras technológiák I*. Edutus Főiskola, Budapest, 2012. 10.

[4] Kyung-Min H., Yung C. S.: *Prospects of laser welding technology in the automotive industry: A review.* Journal of Materials Processing Technology, 245. (2017) 52–54. https://doi.org/10.1016/j.jmatprotec.2017.02.008

[5] Akhter R., Steen W. M., Cruciani D.: *Laser welding of zinc coated steel.* Proceedings of 6th International Conference Lasers in Manufacturing (1989), 105–120.

[6] Chen G., Mei L., Zhang M., Zhang Y., Wang Z.: *Research on key influence factors of laser overlap welding of automobile body galvanized steel.* Optics & Laser Technology, 45/1. (2013) 726–733. https://doi.org/10.1016/j.optlastec.2012.05.002

[7] Chen H. C., Pinkerton A. J., Li, L. Liu Z., Mistry A. T.: *Gap-free fibre laser welding of Zn-coated steel on Al alloy for light-weight automotive applications.* Materials & Design, 32/2. (2011) 495–504. https://doi.org/10.1016/j.matdes.2010.08.034

[8] Chen W., Ackerson P. , Molian P.: *CO_2 laser welding of galvanized steel sheets using vent holes*. Materials & Design, 30/2. (2009) 245–251. https://doi.org/10.1016/j.matdes.2008.05.009

[9] Graham M. P., Kerr H. W., Weckman D. C.: *Laser welding of Zn-coated sheet steels*, Proceedings of SPIE, 2703. (1996) 170–180.

[10] Graham M. P., Hirak D. M., Kerr H. W., Weckman D. C.: *Nd:YAG laser welding of coated sheet steel.* Journal of Laser Applications, 6/4. (1994) 212–222. https://doi.org/10.2351/1.4745359

[11] Gu H.: *Laser lap welding of zinc coated steel sheet with laser-dimple technology.* Journal of Laser Applications, 22/3. (2010) 87–89. https://doi.org/10.2351/1.3485596

[12] Lee S. J., Katayama S., Kawahito Y., Kinoshita K., Kim J. D.: *Weldability and keyhole behavior of Zn-coated steel in remote welding using disk laser with scanner head.* Journal of Laser Applications, 25/3. (2013) 032008. https://doi.org/10.2351/1.4795456

[13] Mei L., Chen G., Yan D., Xie D., Ge X., Zhang M.: *Impact of inter-sheet gaps on laser overlap welding performance for galvanised steel.* Journal of Materials Processing Technology, 226. (2015) 157–168. https://doi.org/10.1016/j.jmatprotec.2015.07.020

[14] Bley H., Weyand L., Luft A.: *An alternative approach for the cost-efficient laser welding of zinc-coated sheet metal.* CIRP Annals, 56/1. (2007) 17–20. https://doi.org/10.1016/j.cirp.2007.05.006

[15] Pieters R. R. G. M., Bakels J. G., Hermans M. J. M., Den Ouden G.: *Laser welding of zinc coated steels in an edge lap configuration.* Journal of Laser Applications, 18/3. (2006) 199–204. https://doi.org/10.2351/1.2227022

[16] Iqbal S., Gualini M. M., Rehman A.: *Dual beam method for laser welding of galvanized steel: experimentation and prospects.* Optics & Laser Technology, 42/1. (2010) 93–98. https://doi.org/10.1016/j.optlastec.2009.05.009

[17] Li X., Lawson S., Zhou Y., Goodwin F.: *Novel technique for laser lap welding of zinc coated sheet steels.* Journal of Laser Applications, 19/4. (2007) 259–264. https://doi.org/10.2351/1.2795755

[18] Yih-fong T.: *Gap-free lap welding of zinc-coated steel using pulsed CO_2 laser*. International Journal of Advanced Manufacturing Technology, 29/3–4. (2006) 287–295. https://doi.org/10.1007/s00170-005-2522-3

[19] Tzeng Y. F., Chen F. C.: *Effects of operating parameters on the static properties of pulsed laser welded zinc-coated steel.* International Journal of Advanced Manufacturing Technology, 18/9. (2001) 641–647. https://doi.org/10.1007/s001700170024

[20] Ma J., Harooni M., Carlson B., Kovacevic R.: *Dissimilar joining of galvanized high-strength steel to aluminum alloy in a zero-gap lap joint configuration by two-pass laser welding.* Materials & Design, 58. (2014) 390–401. https://doi.org/10.1016/j.matdes.2014.01.046

[21] Ma J., Kong F., Carlson B., Kovacevic R.: *Two-pass laser welding of galvanized high-strength dual-phase steel for a zero-gap lap joint configuration.* Journal of Materials Processing Technology, 213/3. (2013) 495–507. https://doi.org/10.1016/j.jmatprotec.2012.10.019

[22] Yang S., Kovacevic R.: *Laser welding of galvanized DP980 steel assisted by the GTAW preheating in a gap-free lap joint configuration.* Journal of Laser Applications, 21/3. (2009) 139–148. https://doi.org/10.2351/1.3184432

[23] Milberg J., Trautmann A.: *Defect-free joining of zinc-coated steels by bifocal hybrid laser welding.* Production Engineering, 3/1. (2009) 9–15. https://doi.org/10.1007/s11740-008-0140-2

[24] Kovács T.: *Laser Welding Process Specification Base on Welding Theories*. Procedia Manufacturing, 22. (2018) 147–153. https://doi.org/10.1016/j.promfg.2018.03.023

Acta Materialia Transylvanica 1/2. (2018) 105–109.
https://doi.org/10.2478/amt-2018-0040,
Hungarian: ~~https://doi.org/10.2478/amt-2018-0039~~
https://doi.org/10.33923/amt-2018-0039
Corrected: 29.08.2023.

Mechanical Studies of Injection Molded Composites with Polypropilene Matrix

Ráthy Istvánné,[1] Pinke Péter,[2] Huszák Csenge[3]

Óbuda University, Donát Bánki Faculty of Mechanical and Safety Engineering, Institute of Materials and Manufacturing Sciences, Department of Materials Technology, Budapest, Hungary

[1] *rathy.istvanne@bgk.uni-obuda.hu*

[2] *pinke.peter@bgk.uni-obuda.hu*

[3] *huszak.csenge@bgk.uni-obuda.hu*

Abstract

The wide use of composite materials is mainly due to their excellent strength / mass ratio, corrosion resistance and relatively low price. Approximately 35-40% of the fibre-reinforced composites are made of thermoplastic polymers in which fibreglass, carbon or natural fibres are most often used as reinforcement, while the remaining 60 – 65% is made up of high-tech carbon or glass fibre-reinforced thermosetting composites. Most of them are used in the transport and electronics industries. New processing technologies not only improve the properties of the products but also contribute to reducing costs.
In this paper, we compare the results of mechanical tests with molded standard specimens with polypropylene matrix and test results from cut-outs from injection molded products.

Keywords*: polypropylene, composites, mechanical properties.*

---

1. Introduction

Plastics are now an integral part of our lives, we use them regularly in the home, the workplace, in industry and in agriculture. The production and use of plastics continues to grow all over the world. One of the leading sectors in the plastics and processing industry is injection molding, whose cash flow is estimated to reach USD 252 trillion by 2018 [1]. The widespread use of plastic based composite materials is primarily due to the excellent strength/mass ratio, the corrosion resistance and the relatively low price of composites [2].

2. Mechanical testing

In practice, the materials have to support various loads during use. The mechanical properties of the base materials are also tested according to stresses; furthermore we choose the base material to meet the requirements of the component for a particular application. The numerical values of the mechanical properties of a particular structural material are generally found in the literature. However, in many cases too much emphasis is placed on the strength of different types and grades of polymers, and from the point of view of end use, It is not only the mechanical properties that are important. In the practical use of polymers, we can rarely ignore other unfavourable factors affecting a given substance. These include environmental influences and temperature. Temperature significantly affects all the properties of the polymers. As a comparison basis, the characteristics measured at room temperature are usually used. Mechanical properties are strongly influenced by the temperature, depending on the type of polymer. There may be differences between these types of polymer depending on the brand name and the type designation [3]. A question arises concerning different mechanical test results performed on composite specimens from serial production conditions, relating to the results of the standard test specimens. In our article, we have tried to formulate answers to this question.

2.1. Tensile testing

The aim of the tensile test of polymers is to determine the resistance of the material against tensile load, the tensile strength. The course of the test, the shape, the size of the specimen, the acquisition and evaluation of the experimental results are defined in the standard of MSZ EN ISO 527-1: 2012 [4]. The test was carried out on a Zwick Z050 type tensile testing machine. Since the shape of the product did not allow the use of a standard cross-section, the tensile specimens cut from the injection molded PP+30% glass fibre products, were rectangular cross-section (2x15 mm).

The specimens ruptured with minimal elongation, this was almost a brittle fracture (**Figure 1.**). Altogether 10 test work pieces were tensile tensed at room temperature.

We define the tensile strength with the following formula:

$$R_m = \frac{F_{\max}}{S_0} \quad \text{(MPa)} \tag{1}$$

where F_{max} is the maximum tensile force (N), S_0 is the initial cross section of the test piece (mm^2).

The measured tensile strength was varied between 63–71 MPa. The tensile curves recorded during the tests are shown in **Figure 2.**

According to literature data, the 30% short glass fibre reinforced polypropylene composite has a tensile strength of 82 MPa.

The engineering strain values varied ε=3,6–4,1%, which were determined by the following relationship:

$$\varepsilon = \frac{L_U - L_0}{L_0} 100 \quad (\%) \tag{2}$$

where L_0 is the original gauge length, L_u is the final gauge length.

According to literature data, the 30% short-fiber polypropylene composite strength is R_m = 82 MPa, the engineering strain value is ε = 4.9 % [3].

The difference between the measured values and the literature data is derived from the potential differences in the additives between the examined PP matrix and the literature PP matrix.

At the same time, tests were carried out on standard specimens, which were cut out from PP+30% fiberglass composite material. The maximal forces distribution is shown the **Figure 3.**

In this case the tensile strength varied R_m = 79–81 MPa, the engineering strain value was ε = 4.83% These values are very close to the literature data.

The fractured surface was examined with an electron microscope (**Figure 4.**). The PP base material is visibly adhering to the surface of the glass fibres. The base matrix and the glass fibre together ensures the capacity.

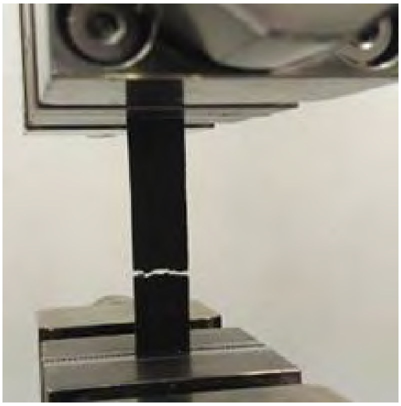

Figure 1. *Tensile specimen after fracture*

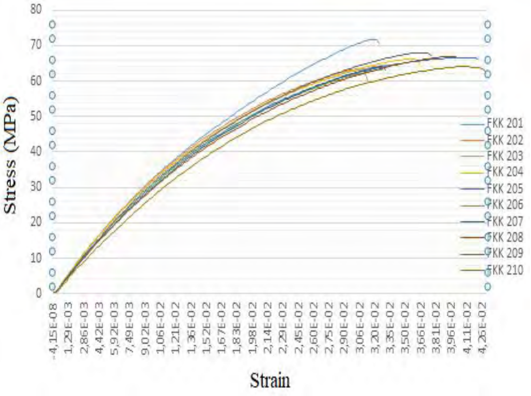

Figure 2. *Tensile graphs of the specimens*

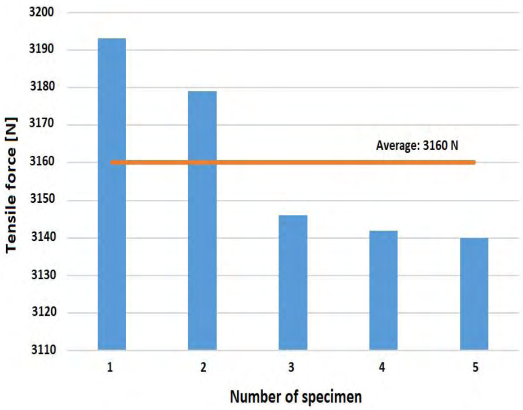

Figure 3. *Distribution of maximum forces*

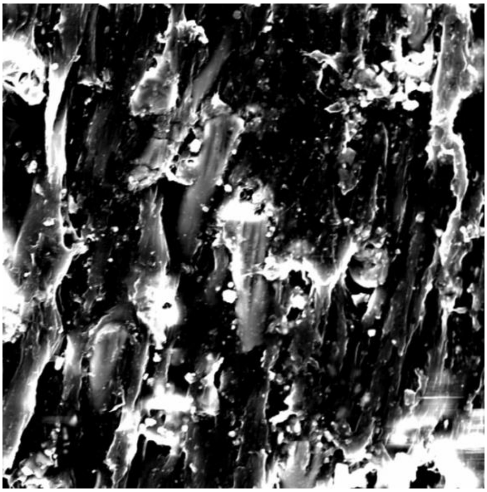

Figure 4. *Electron microscopy of the fractured surface*

2.2. Bending test

Polymers and polymer matrix composites are often characterized by bending tests. The prismatic sample is placed horizontally across two supports and then a force applied to the top of the midpoint. During the test, the load starts from zero and increases steadily until the sample is fractured. Meanwhile, the force (*F*) and the deflection (*f*) are measured in the middle of the test. The deformation of the test specimen can be deduced from the deflection and the magnitude of the force [3]. Results are shown in **Figure 5.**

The following formula was used to determine the bending strength with the maximum bending torque:

$$R_{mh} = \frac{3 \cdot F_{\max} \cdot L}{2 \cdot B \cdot H^2} \quad (MPa) \tag{3}$$

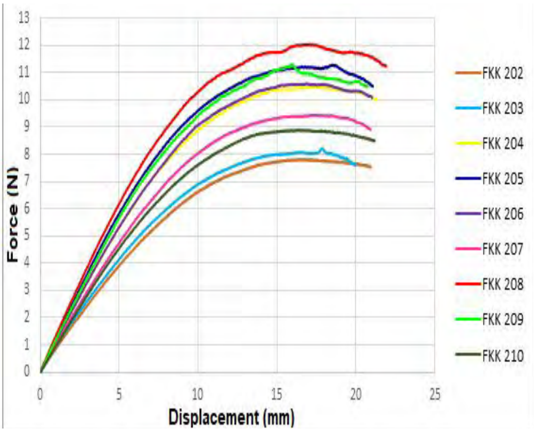

Figure 5. *The loading force-bending diagram*

The bending modulus of elasticity was calculated using the following formula:

$$E = \frac{\Delta F L^3}{4 \Delta f B H^3} \quad (GPa) \tag{4}$$

The test (**Figure 6.**) was carried out by an Instron 5965 machine and was performed according to MSZ EN ISO 178:2011. The marking, the sizes, the calculated bending strength and flexural modulus values for the specimens are given in **Table 1.**

The bending strength of polypropylene without fiberglass was 37 MPa, the flexural modulus was 1.4 GPa. The polypropylene with 30% short-fiber specimen cut out of an injection molded product showed a flexural modulus of 52–59 MPa. In the literature a flexural strength of 120 MPa, and a flexural modulus of 6 GPa are published for PP+30% GF (glass fibre) composites.

Table 1. *Flexural strength and Young's modulus values determined by the tests*

Notation	Fmax (N)	L (mm)	B (mm)	H (mm)	σ (MPa)	R (MPa)
FKK 202	7.8	70	7.61	1.43	52.6	1799.1
FKK 203	8.2	70	7.69	1.44	54.0	1714.3
FKK 204	8.9	70	7.91	1.50	52.5	1665.0
FKK 205	11.3	70	8.25	1.56	59.1	1674.2
FKK 206	10.6	70	8.30	1.53	57.3	1815.2
FKK 207	9.4	70	8.06	1.51	53.7	1662.7
FKK 208	12	70	8.34	1.59	59.8	1798.2
FKK 209	11.3	70	8.29	1.55	59.6	1965.4
FKK 210	10.5	70	8.21	1.53	57.4	1848.7
Átlag					56.2	1771.4

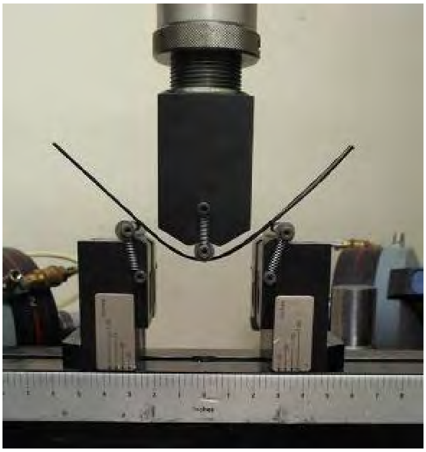

Figure 6. *The sample in bending test*

The average of the bending strength values is shown in Figure 7.

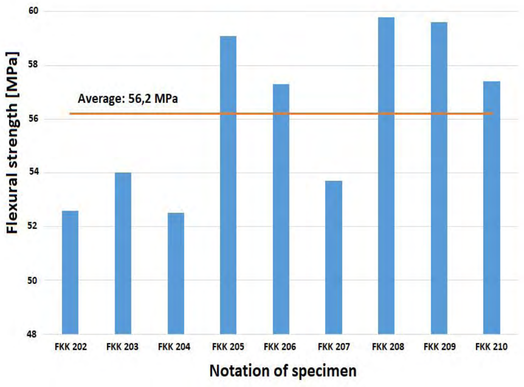

Figure 7. *The bending strength values*

2.3. Impact test

Methods for Dynamic Material testing provide a solution for the determination of loads that cause fracture, and the toughness of the particular structural material. In the case of polymers, toughness relates to their energy absorbing ability. For structural materials, it can be stated that the material with higher impact energy has a higher toughness. The test may be carried out with notched and non-notched specimens [4]. The specimens we used were non-notched. We employed a Charpy Impact Testing Machine according to MSZ EN ISO 179-1:2010. The dimensions of the specimens are shown in Table 2.

AThe Charpy impact toughness measured on the polypropylene based 30% glass fiber reinforced composite with a non-notched specimen was 4 J/cm^2 [5], this is equal to 40 kJ/m^2.

Table 2. *Impact test sample sizes*

Sign of work-piece	Width (mm)	Thickness (mm)	A (mm^2)
FKK 202	3.89	3.81	14.8209
FKK 203	3.95	3.71	14.6545
FKK 204	3.85	3.79	14.5915
FKK 205	3.82	3.79	14.4778
FKK 206	3.84	3.86	14.8224
FKK 207	3.81	3.76	14.3256
FKK 208	3.71	3.86	14,3206
FKK 209	3.84	3.81	14.6304
FKK 210	3.70	3.85	14.2450

The values we measured and calculated are shown in Table 3. The impact toughness values are between 27–36 KJ/m^2.

The average is shown in Figure 8.

These results compare well with the literature data.

Table 3. *Impact test and impact strength value*

Sign of work-piece	Absorbed energy (J)	Impact strength (kJ/m^2)
FKK 202	0.46	31
FKK 203	0.41	28
FKK 204	0.40	27
FKK 205	0.52	35
FKK 206	0.52	35
FKK 207	0.48	33
FKK 208	0.47	32
FKK 209	0.53	36
FKK 210	0.45	32

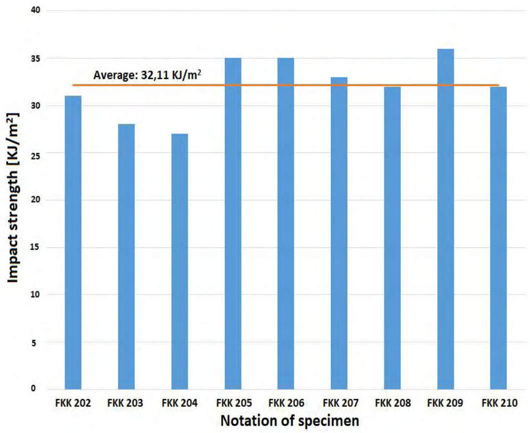

Figure 8. *The average of the impact strength values*

3. Conclusion

Mechanical tests were performed with specimens cut from workpieces produced in series production in industrial conditions. We find that the magnitudes of the tensile test results are consistent with the results of experiments with standard test specimens, but they show lesser values. This may be the effect of additives not known to us in these industrial products.

Bending tests showed greater differences between the measured and the literature data, this can be explained by the difference in PP matrix additives. The impact test results are well-aligned with the literature data.

References

[1] Transparency Market Research: *Injection Molded Plastics Market – Global Industry Analysis, Size, Share, Growth and Forecast, 2010-2018.* https://pitchengine.com/pitches/8f64cc4f-8df4-4314-9eeb-5e9c534da54d (accessed 1.03.2017)

[2] Kar K. K. (ed.): *Composite Materials: Processing, Applications, Characterizations.* Springer Verlag, Berlin–Heidelberg, 2017. https://doi.org/10.1007/978-3-662-49514-8

[3] Szakács H., Varga Cs., Nagy R.: *Polimerek méréstechnikája.* Pannon University, Veszprém, 2012. 71–76.

[4] Varga Cs.: *Műszaki műanyagok. part 2.* Pannon University, Veszprém, 2012. 24.

[5] Czél Gy., Kollár, M.: *Anyagvizsgálati praktikum.* Sunplant Kft., 2009. 36.

ACTA MATERIALIA TRANSYLVANICA 2018

ERRATUM

Az Erdélyi Múzeum-Egyesület mint kiadó és az Acta Materialia Transylvanica szerkesztősége sajnálattal értesíti a szerzőket és az olvasókat, hogy a folyóirat 2018-as évfolyam 1 és 2. lapszámaiban a cikkek magyar nyelvű változatainál a DOI-azonosítók prefixei hibásan jelentek meg.

A cikkek fejléceiben a magyar nyelvű változatnak megfelelő DOI prefix helyesen: **10.33923**, nem 10.2478.

A prefixek 2023 szeptemberében a lapszámok honlapján:

https://eme.ro/publication-hu/acta-mat/acta2018-1.htm illetve

https://eme.ro/publication/acta-mat/acta2018-1.htm

és

https://eme.ro/publication-hu/acta-mat/acta2018-2.htm illetve

https://eme.ro/publication/acta-mat/acta2018-2.htm

minden cikkben javításra kerültek, feltüntetve az eredeti, hibás és az új, helyes azonosítót is.

A DOI-azonosítók helyes számra történő cserélése a Magyar Tudományos Művek Tárában (MTMT) is megtörtént.

A hibáért minden szerző és olvasó szíves elnézését kérjük és tisztelettel kérjük, hogy ezentúl az új, helyes azonosítót legyenek szívesek használni!

Az Erdélyi Múzeum-Egyesület Kiadó és az Acta Materialia Transylvanica Szerkesztősége nevében:

Bitay Enikő

főszerkesztő

Kolozsvár, 2023. 09. 01.

ACTA MATERIALIA TRANSYLVANICA 2018

ERRATUM

The Erdélyi Múzeum-Egyesület as Publisher, and the Editorial Office of Acta Materialia Transylvanica regret to inform the authors and readers that the prefixes of the DOI identifiers of the Hungarian versions of the articles in issues 1 and 2 of the journal in 2018 were incorrectly published.

In the article headings, the DOI prefix corresponding to the Hungarian version of the article is **10.33923**, not 10.2478.

In September 2023, the prefixes were corrected in all articles on the websites of the journal issues:

https://eme.ro/publication-hu/acta-mat/acta2018-1.htm respectively

https://eme.ro/publication/acta-mat/acta2018-1.htm

and

https://eme.ro/publication-hu/acta-mat/acta2018-2.htm respectively

https://eme.ro/publication/acta-mat/acta2018-2.htm

showing the original incorrect one crossed out and the new, correct identifier.

The replacement of the DOI identifiers with the correct number has also been done in the Hungarian Repository of Scientific Works (MTMT).

We apologize to all authors and readers for this error, and respectfully request that you use the new, correct identifier from now on!

On behalf of the Erdélyi Múzeum-Egyesület Publisher and the Editorial Office of Acta Materialia Transylvanica:

Bitay Enikő
Editor-in Chief

Cluj-Napoca, 1st September, 2023.